China Geology 8 (2025) 779−796

China Geology

Journal homepage: http://chinageology.cgs.cn
https://www.sciencedirect.com/journal/china-geology

Late Jurassic tectono-volcanic evolution and sauropod radiation of eastern Jiangnan orogen: Evidence from Tunxi Formation, China

Xin-xin Ren[a,*], Xu-ri Wang[a], Yi-chuan Liu[a], Shu-bin Ju[b]

[a] *Key Laboratory of Stratigraphy and Paleontology of the Ministry of Natural Resources*, *Institute of Geology*, *Chinese Academy of Geological Sciences*, *Beijing* 100037, *China*
[b] *Dalian Natural History Museum*, *Dalian* 116023, *China*

ARTICLE INFO

Article history:
Received 9 August 2023
Received in revised form 29 December 2023
Accepted 8 January 2024
Available online 11 November 2024

Keywords:
Sauropod dinosaur
Mamenchisaurid
Volcanic activity
Dinosaur evolution radiation
Subduction plate
Tunxi Formation
Eastern China

ABSTRACT

A prevailing theory suggests that volcanic eruptions triggered environmental changes, which compelled dinosaurs to migrate in search of new habitats. Compelling evidence for this hypothesis has now been discovered in the Tunxi Basin of eastern China. During the Late Mesozoic, the subduction of the Pacific Plate beneath southeastern China led to multi-stage volcanic activity. The Tunxi Formation in the basin, the first reported Upper Jurassic volcanic unit in the eastern Jiangnan orogen. It overlies the stratum bearing the easternmost mamenchisaurids, which is the dominant Asian sauropod lineage. Geochemical analyses suggest its affinity with coeval magmatism in southeastern China, while new rhyolite zircon U-Pb dating yields an age of 151.6 ± 2.2 Ma, further indicating a transition from arc magmatism to back-arc extension driven by Paleo-Pacific subduction during the Late Jurassic. These studies also confirm that, as early as 156 Ma, the Tunxi Basin was already a key habitat for mamenchisaurids. The Late Jurassic subduction of the Paleo-Pacific Plate caused extensive magmatism across eastern China. This intense tectonic shift likely induced abrupt environmental changes in relative basins. Severe volcanic activity drastically reduced the habitat of mamenchisaurids, prompting a northwestward and southward radiation trend —presents a coherent scene of volcanic eruptions, environmental catastrophe, and dinosaurs migrating.

1. Introduction

A current consensus is that the paleo-Pacific plate was subducted beneath East Asia during the Late Mesozoic, leading to the formation of massive magmatic rocks and associated major ore deposits along the western Pacific margin, particularly in southeastern China (Yang SY et al., 2021). Consequently, widespread Mesozoic igneous rocks, with outcrops covering an area of about 25×10^4 km^2, have become a distinct feature of southeastern China (Liu JX et al., 2020). Exploring lithologic assemblages and petrogeochemistry would contribute to deeper insights into the subduction of the paleo-Pacific plate and the Late Mesozoic magmatism in southeastern China. Nevertheless, the subduction dynamics and impacts of the paleo-Pacific plate remain controversial.

Previous studies mostly focus on the intrusions in southeastern China except for the volcanic rocks in the volcano-sedimentary basins (e.g., Yang SY et al., 2021). The Tunxi Basin, a volcano-sedimentary basin in the eastern Jiangnan orogen, is situated near the coastal area in southeastern China (Fig. 1). The volcanic sequences in the basin have kept the complete magmatic process, with some representative stratigraphic sections facilitating regional correlation. However, there is a lack of comprehensive studies on the volcanic units in the volcano-sedimentary basins in the eastern Jiangnan orogen.

Previous studies (e.g., Wang QH, 2001) suggest that the former Upper Jurassic volcanic sequences in the Anhui-Zhejiang region were formed during the Lower Cretaceous, with the absence of the Upper Jurassic strata (Chen PJ, 2000). The Tunxi Formation is the first reported Upper Jurassic volcanic unit in the Jiangnan orogen in eastern China (e.g., Ren XX et al., 2015, 2017; Tang S et al., 2016; Yu XQ et al., 2016).

Additionally, fossils of the sauropod dinosaurs of genera

* Corresponding author: *E-mail address*: laotourenxin@126.com (Xin-xin Ren).

Literary editor: Xi-jie Chen
doi:10.31035/cg2023087
2096-5192/© 2025 China Geology Editorial Office.

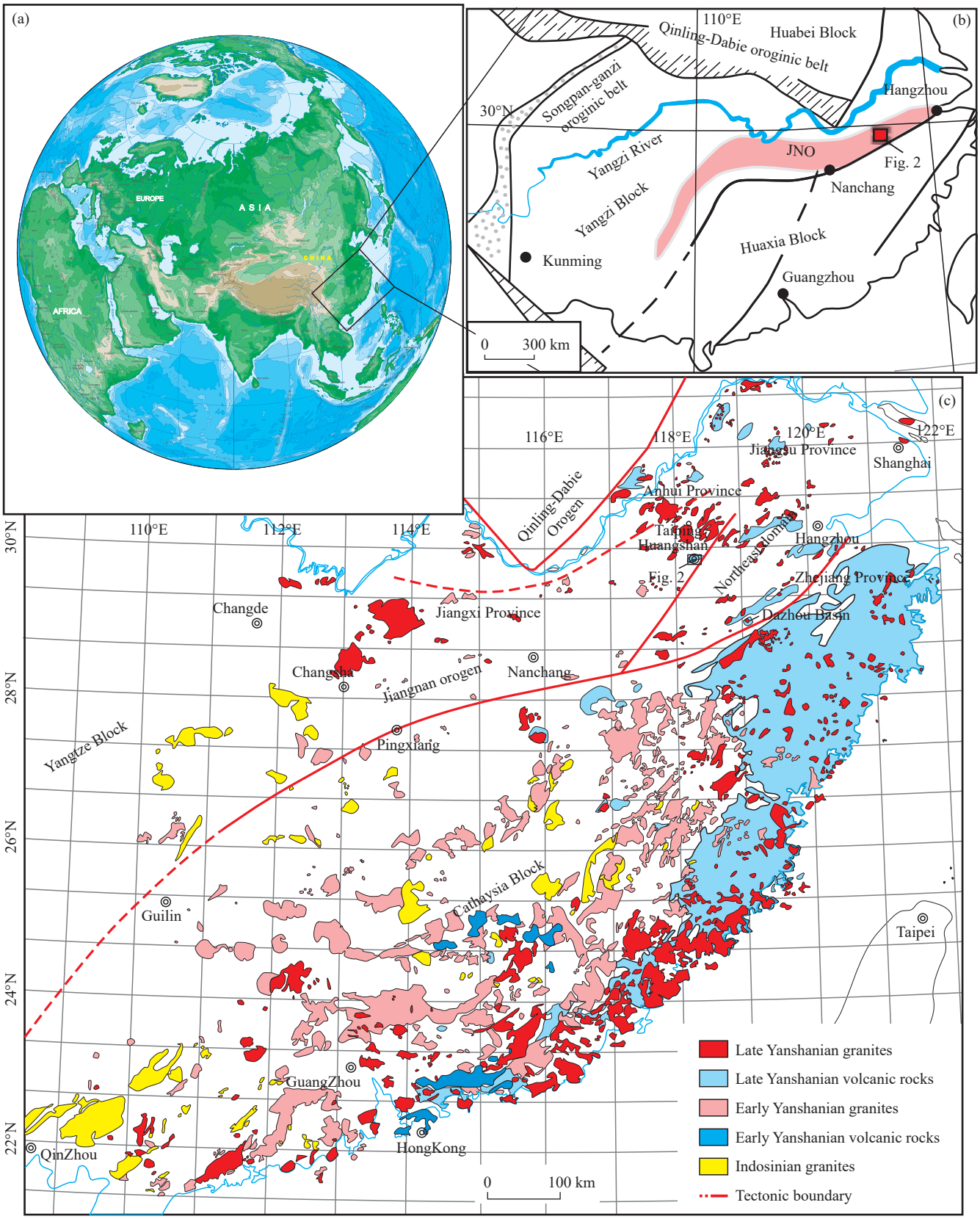

Fig. 1. Mesozoic granites and volcanic rocks distributed in southern China (modified from Yang SY et al., 2021). JNO–Jiangnan orogen.

Huangshanlong anhuiensis and *Anhuilong diboensis* were excavated in the Hongqin Formation, which underlies the Tunxi Formation (e.g., Huang JD et al., 2014; Ren XX et al., 2018). The dinosaurs of both genera are phylogenetically categorized as mamenchisaurids (Ren XX et al., 2018). China is well known for its diverse array of eusauropod dinosaur fossil-bearing strata such as the Shaximiao Formation in southwestern China (e.g., Peng GZ et al., 2019; Ren XX et al.,

2022, 2023). Among these, Mamenchisauridae (Young CC and Chao XJ, 1972) serves as a significant clade for research into the evolution of Asian sauropod dinosaurs (e.g., Young CC, 1939; Ouyang H, 1989; Fang XS et al., 2004; Jiang S et al., 2011; Xing LD et al., 2015; Ren XX et al., 2021), emerging as the most prosperous non-neosauropodan sauropod clade predominating East Asia (e.g., Xing LD et al., 2015; Ren XX et al., 2018; Moore AJ et al., 2023). The fauna of mamenchisaurid dinosaurs, traditionally determined at the Middle-Late Jurassic ages, includes 14 genera (consisting of 28 species) from China, two from Africa, and one from Australia (e.g., Huang JD et al., 2014; Xing LD et al., 2015; Ren XX et al., 2018; Mannion PD et al., 2019; Ren XX et al., 2021; Moore AJ et al., 2023). However, following the two dispersive Middle Jurassic mamenchisaurid genera in Anhui Province, no mamenchisaurid genus in the Late Jurassic sediments in eastern China has been reported.

This study aims to gain a more comprehensive understanding of the newly discovered Upper Jurassic Tunxi Formation in the study area using methods combining petrology, stratigraphy, geochemistry, zircon chronology, and Hf isotopes, including zircon U-Pb dating, zircon Hf isotopic composition analysis, and the geochemistry of whole-rock major and trace elements. To this end, this study determines the regional eruption ages and their spatiotemporal distributions, as well as the petrogenesis. Furthermore, it provides novel insights into the evolutionary process of the subduction of the paleo-Pacific plate in the eastern Jiangnan orogen, revealing the geological implications of the subduction for the evolution of Mamenchisauridae in eastern China. Additionally, this study determines the exact age of the mamenchisaurid fossil-bearing unit in eastern China.

2. Geological setting

The South China Block consists of the Yangtze and Cathaysia blocks (Wang Q et al., 2006). The NW-trending Jiangnan orogen, measuring over 1500 km in length and 120 km in south, was formed due to the collision between the Yangtze and Cathaysia blocks during the Neoproterozoic (e.g., Zhao JH et al., 2011). During the Late Mesozoic, this orogen, under the control of the Tethyan tectonic domain, progressively transformed into the Pacific tectonic domain, during which many NNE-trending strike-slip faults were formed and extensive intrusions and eruptions of intermediate magmas occurred (Zhu G and Liu GS, 2000; Fig. 1). Concurrently, significant magmatism occurred in the Cathaysia block (Fig. 1). The Jiangnan orogen is located at the junction of the Yangtze and Cathaysia blocks, with volcanic units distributed principally in volcanic basins along this orogen and its adjacent areas (e.g., the coastal area in southeastern China; Fig. 1).

The Tunxi Basin in eastern China, a volcano-sedimentary basin in the eastern Jiangnan orogen (Jiang LL et al., 2016), was formed during the Mesozoic. This basin exhibits well-developed continental red beds with continuous outcrops. The Jurassic strata in the basin include the Lower Jurassic Yuetan Formation, the Middle Jurassic Hongqin Formation, and the Upper Jurassic Tunxi Formation (Ren XX et al., 2015, 2017). Among them, the Hongqin Formation is reported to contain the only horizon bearing the fossils of mamenchisaurid dinosaurs in eastern China (Wang Q et al., 2006; Huang JD et al., 2014; Ren XX et al., 2018, 2021). Previous studies on 1:50000 geological surveys of this basin referred to this formation as the Lower Cretaceous Siling Formation (Ren XX et al., 2015; Tang S et al., 2016; Yu XQ et al., 2016). Recent studies focus primarily on the zircon U-Pb ages of this formation (Ren XX et al., 2015; Tang S et al., 2016; Yu XQ et al., 2016).

The Jurassic volcano-sedimentary sequences in the Tunxi Basin are dominated by sandstones and mudstones interbedded with volcanic rocks. They can be classified into the Lower Jurassic Yuetan Formation (dominated by conglomerates, sandstones, and mudstones), the Middle Jurassic Hongqin Formation (consisting primarily of sandstones and mudstones), and the Upper Jurassic Tunxi Formation (Ren XX et al., 2017). Based on the Jurassic dinosaur fossils excavated in 2002, two mamenchisaurid genera have been reported in the Hongqin Formation (Wang Q et al., 2006; Huang JD et al., 2014; Ren XX et al., 2015, 2017, 2018). The Tunxi Formation in the study area occurs primarily at Huangkou, Youxi, and Sanchong villages, covering an area of approximately 5 km^2 (Fig. 2).

3. Samples and methods

Petrology in this study highlights the distribution of volcanic rocks in the Tunxi Formation within the study area, with the holostratotype of mineral associations and volcanic eruption sequences being further investigated (Fig. 3). Geochemical samples collected from the Tunxi Formation in the Tunxi Basin (Fig. 4) included four rhyolitic samples from Sanchong Village and six samples from the holostratotype at Huangkou Village (Supplementary Table 1). The four rhyolitic samples comprised TW03-T01, TW03-T02, TW04-T01, and TW04-T02, while the six samples were TW01-B02 (tufflava) from layer 2, TW01-B03 (crystal tuff) from layer 3, TW01-B04 (tufflava) from layer 4, TW01-B05 (volcanic breccia) from layer 5, TW01-B07 (crystal tuff) from layer 7, and TW01-B11 (rhyolite) from layer 11 (Fig. 4). The microscopic identification was completed at the Anhui Institute of Geological Experiments (Hefei Mineral Resources Supervision and Testing Center, Ministry of Land and Resources). All these samples were massive in shape, exhibiting porphyritic textures and massive structures (Fig. 5). For chemical analyses, whole-rock powders were prepared by grinding cleaned samples to 200 mesh using a ceramic ball mill.

3.1. Major and trace elements

All ten samples were dated at the ALS Chemex (Guangzhou) Co., Ltd.. Their major elements were measured using an X-ray fluorescence (XRF) spectrometer and fused glass disks following Goto A and Tatsumi Y (1996). Their

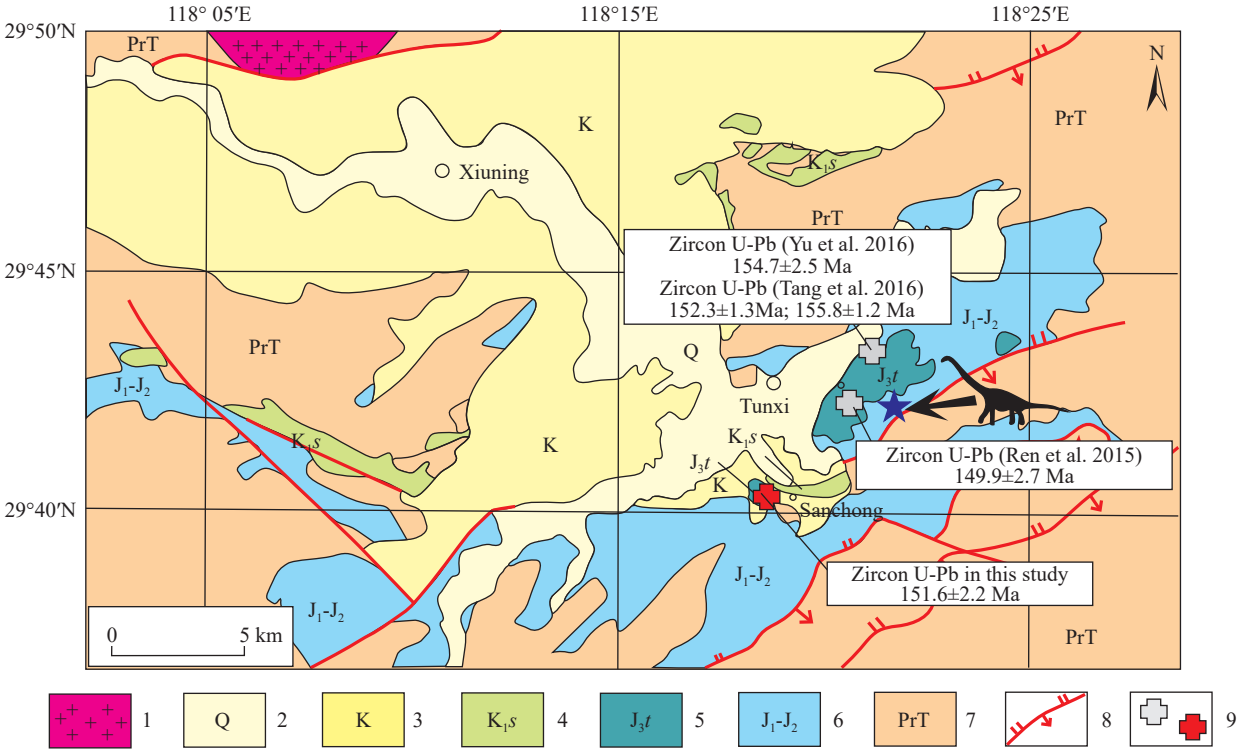

Fig. 2. Geological map of the Tunxi area, Huangshan City (modified from a 1∶50000 geological map; the Middle Jurassic dinosaur quarry denoted by a purple star and dinosaur silhouette). 1–Pre-Sinian intrusion; 2–Quaternary; 3–Cretaceous unit without the Shiling Formation; 4–Early Cretaceous Shiling Formation; 5–Late Jurassic Tunxi Formation; 6–Lower-Middle Jurassic unit; 7–Pre-Triassic; 8–Measured thrust fault; 9–Sampling site (gray: previous studies; yellow: this study).

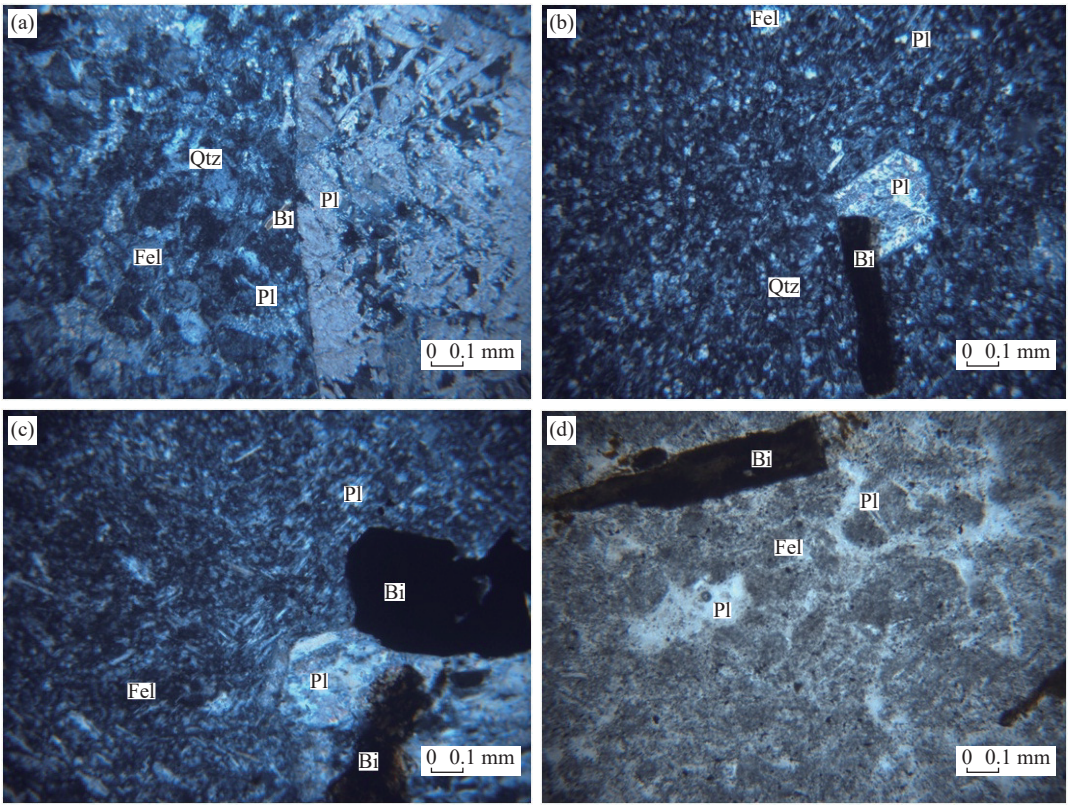

Fig. 3. Photomicrographs of volcanic rocks from the Tunxi Formation. a–Photomicrograph of volcanic breccias from layer 5 (porphyritic and spherulitic textures); b–photomicrograph of tufflavas from layer 8 (porphyritic and pilotaxitic textures); c–photomicrograph of tufflavas from layer 10 (porphyritic and pilotaxitic textures); d–photomicrograph of spherulitic rhyolites from layer 11 (porphyritic and spherulitic textures). Bi–biotite; Fel–felsic; Pl–plagioclase; Qtz–quartz.

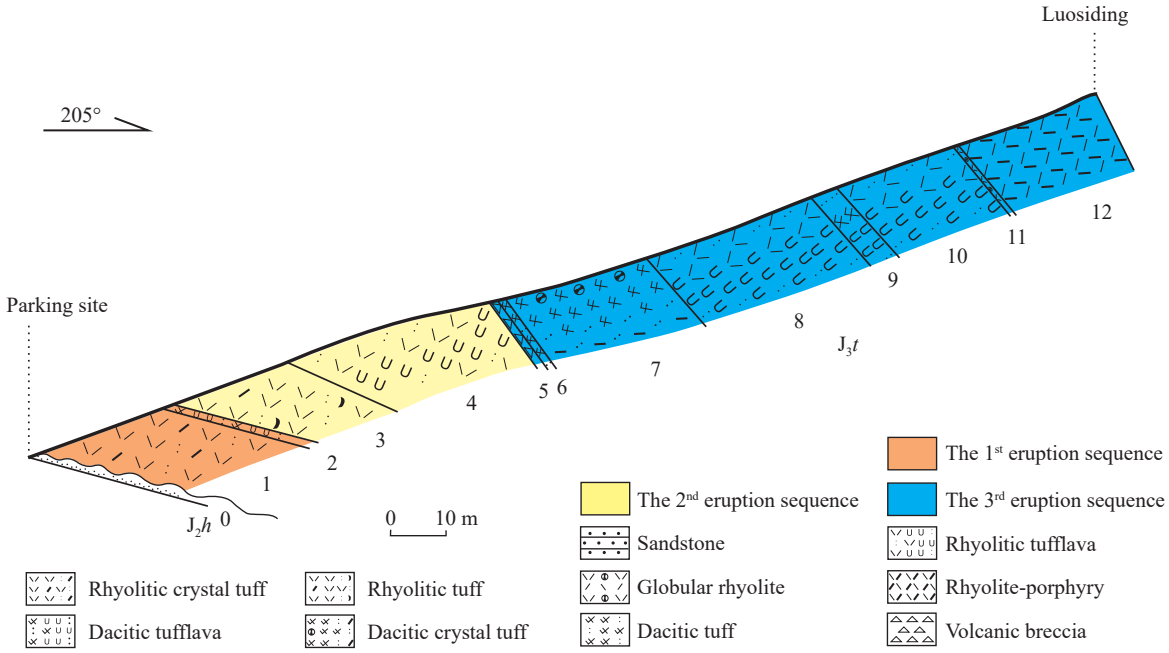

Fig. 4. Measured profile of the Tunxi Formation in Huangkou, Tunxi area, Huangshan City. Orange: the 1st sequence; yellow: the 2nd sequence; blue: the 3rd sequence.

trace elements were determined using an inductively coupled plasma mass spectrometer (ICP-MS) following Liu Y et al., 2007.

3.2. U-Pb dating

Sample WN12-T (original number: TW04-T02) from Sanchong Village was dated. Zircon grains were separated from this sample using standard density and magnetic separation techniques at the Hebei Regional Geological Survey in Langfang City. Their cathodoluminescence (CL) images were obtained using a JEOL scanning electron microscope operating at 15 kV and 4 nA at the Beijing Zirconia Pilot Technology Co., Ltd. The zircon U-Pb isotopic analysis, based on the laser ablation inductively coupled plasma mass spectrometry (LA-ICP-MS), was conducted using an Agilent 7500a laser ablation system at the LA-ICP-MS laboratory in the Hefei University of Technology (HFUT). Detailed operating conditions of the laser ablation system and the ICP-MS instrument, as well as data reduction, are stated in Liu YS et al. (2010). To monitor the instrument stability and the accuracy of ion counting statistics, measurements were carried out every eight measurement points combined with a certified reference material sample. After the analyses, the $^{206}Pb/^{238}U$, $^{207}Pb/^{206}Pb$, $^{207}Pb/^{235}U$, and $^{208}Pb/^{232}Th$ ratios were calculated using the GLITTER v.4.4 software, followed by a common lead correction (Andersen T, 2002). The weighted average U-Pb ages and Concordia diagrams were determined using Isoplot 3.0, quoted at 1σ uncertainty and 90% confidence level (Ludwig KR, 2003).

3.3. Hf isotopes

Eighteen samples, namely WN12-T-04, -06, -08, -12, -14, -18, -19, -26, -30, -32, -34, and -49 and P3-TW01 to -TW06, were dated (Fig. 6). Among these, P3-TW01 to -TW0106 were taken from the holostratotype for the zircon U-Pb isotopic test in 2015 (Ren XX et al., 2015). The *in situ* zircon Hf isotopic analysis was conducted using a Neptune multi-collector inductively coupled plasma mass spectrometer (MC-ICP-MS), a double-focusing instrument allowing for high-resolution measurements in multiple collector modes, at the Institute of Geology and Geophysics (IGG), Chinese Academy of Sciences. The reproducibility and accuracy of Hf measurements using the MC-ICP-MS were assessed based on a 200 ppb JMC 475 Hf standard. For the JMC 475 standard, the average $^{176}Hf/^{177}Hf$ ratio over one year was 0.282158 ± 16 (n = 140, 2s), which can be normalized to $^{179}Hf/^{177}Hf$ = 0.7325 using an exponential law for mass bias correction (Nowell GM et al., 1998). Besides, an ArF excimer laser ablation system was employed for laser-ablation analysis. Data were collected during the 50 s of ablation with a spot size of 40 μm in a static mode. In each step, masses 171, 173, and 175 were simultaneously monitored to correct the isobaric interferences of Lu and Yb isotopes on mass 176. Additionally, ^{176}Yb and ^{176}Lu were calculated assuming a $^{176}Yb/^{173}Yb$ ratio of 0.796179 and a $^{176}Lu/^{175}Lu$ ratio of 0.02655 (Chu NC et al., 2002). The Yb isotope ratios were normalized to $^{173}Yb/^{171}Yb$ = 1.132685 and the Hf isotope ratios to $^{179}Hf/^{177}Hf$ = 0.7325 (Fisher CM et al., 2014) using an exponential law for instrumental mass fractionation (IMF) correction. The IMF of Lu was assumed to align with that of Yb. The aforementioned method provided an accurate correction for the ^{176}Yb interference on ^{176}Hf (e.g., Iizuka T and Hirata T, 2005). Data reduction was performed through the deconvolution of time-resolved data using the Iolite software package v.2.5 (Paton C et al., 2011).

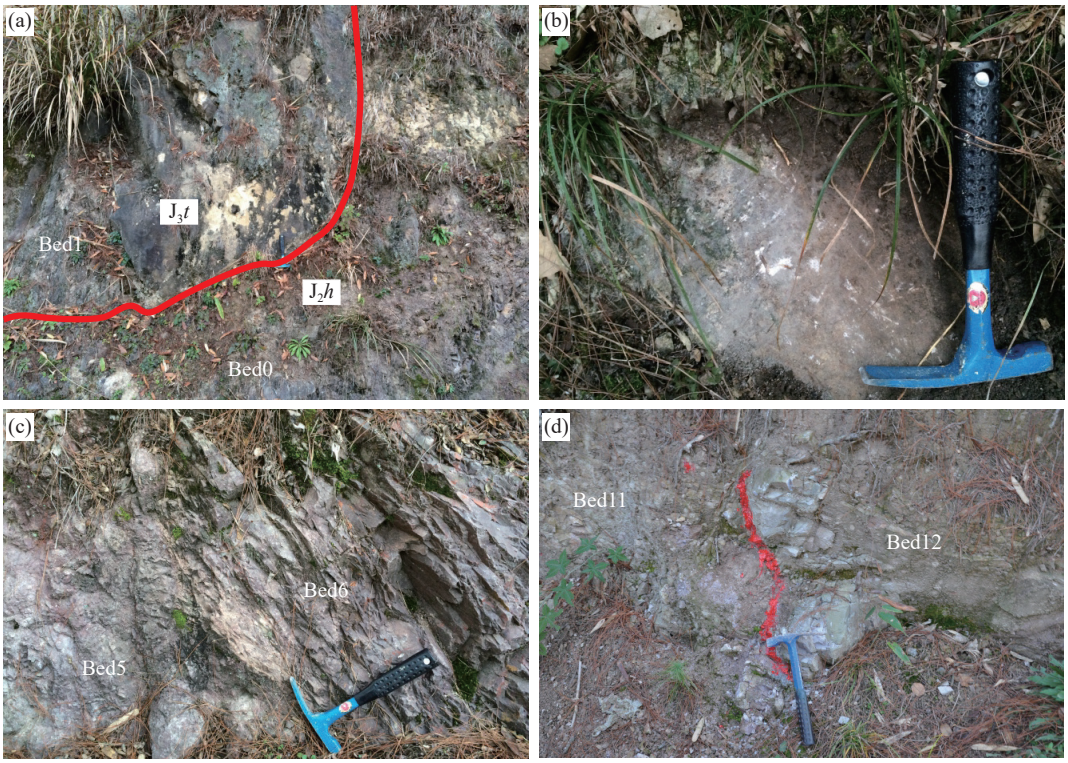

Fig. 5. Field photographs of the holostratotype of the Tunxi Formation in Huangkou, Huangshan City. a–Unconformable contact between the Tunxi (J_3t) and Hongqin (J_2h) formations; b–dacitic tufflavas in the 2nd layer; c–volcanic breccias in the 5th layer and dacitic tuff in the 6th layer; d–spherulitic rhyolites in the 11th layer and rhyolite porphyry in the 12th layer.

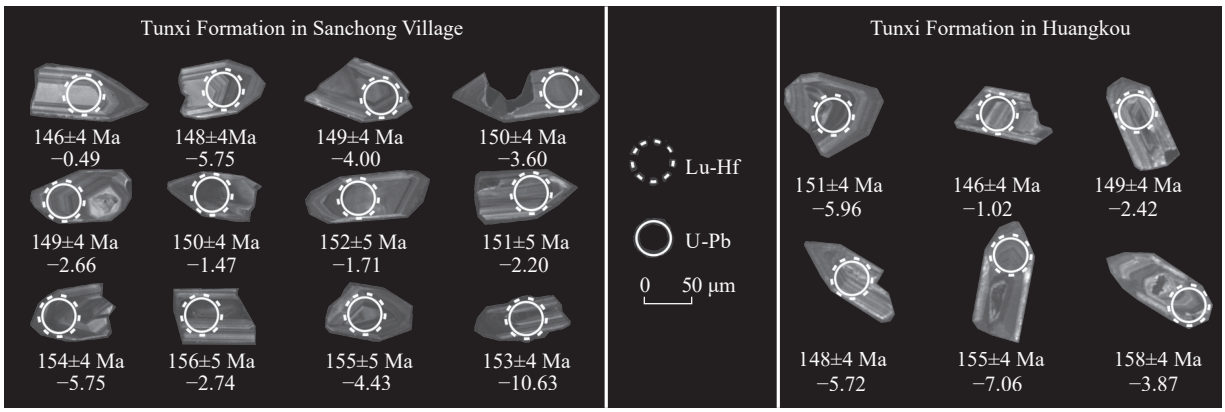

Fig. 6. CL images of zircon grains in samples, with laser spot positions and related $^{206}Pb/^{238}U$ ages and $\varepsilon_{Hf}(t)$ values for U-Pb and Lu-Hf dating. Scale bar = 50 μm.

4. Results

4.1. Petrology

4.1.1. Petrologic features

Two distinct petrologic types of volcanic rocks, i.e., lavas and pyroclastic rocks, were identified in the Tunxi Formation (Table 1).

(i) Lavas

Lavas identified in the Tunxi Formation include rhyolites, rhyolitic tufflavas, and dacitic tufflavas.

The rhyolites exhibit sub-angular to sub-circular detrital feldspar and quartz grains, most of which are well-sorted. They display weak sericite and argillic alterations, with sub-

Table 1. Eruption sequences of the Tunxi Formation in Lusiding, Huangshan City.

Sequence	Thickness /m	Lithology
3	163.8	Rhyolite–porphyry
		Globular rhyolite
		Rhyolitic tufflava
		Dacitic tufflava
		Rhyolitic tufflava
		Dacitic tuff
		Dacitic tuff
		Volcanic breccia
2	47.1	Rhyolitic tufflava
		Rhyolitic tuff
1	34.1	Tufflava
		Rhyolitic tuff

angular to sub-circular lithic debris dispersed in quartziferous grains and phyllites. The quartz grains are cryptocrystalline and exhibit wavy extinction. Secondary chlorites and biotites in rhyolites are tabular in shape, mostly with dark edges. Additionally, biotites contain columnar tourmaline crystals, with fillings composed generally of clay minerals (Fig. 3d).

The rhyolitic tufflavas consist primarily of quartz and feldspar, whose grains are generally angular to sub-angular in shape. The feldspar grains exhibit widespread sericite and argillic alterations. Lithic debris in rhyolitic tufflavas, typically fine-grained, is dominated by mudstones and siliceous minerals. The muscovite, tourmaline, and zircon in them are flaky or granular in shape, and the fillings in them are composed of argillaceous and ferruginous minerals (Fig. 3b).

The dacitic tufflavas exhibit idiomorphic or hypidomorphic tabular plagioclase phenocrysts, with some metasomatized by sericite and clay minerals. The plagioclase grains in the matrix are identified as idiomorphic crystallites. The dacitic tufflavas contain spheroidal felsic phenocrysts, with a minor quantity of quartz phenocrysts distributed between plagioclase and felsic grains. The quartz grains are xenomorphic. Additionally, the dacitic tufflavas manifest xenomorphic granular opaque minerals, being disseminated in the rocks (Fig. 3c).

(ii) Pyroclastic rocks

Pyroclastic rocks found in the Tunxi Formation include tuffs and volcanic breccias.

The tuffs manifest idiomorphic plagioclase phenocrysts with tabular textures, with some metasomatized by sericite and clay minerals. These tuffs contain idiomorphic and tabular biotite with dark edges. Plagioclases in the matrix emerge as idiomorphic and elongated crystallites. Additionally, the tuffs contain spheroidal felsic grains and xenomorphic granular opaque minerals, with xenomorphic granular quartz grains distributed between plagioclase and felsic grains (Fig. 3).

The volcanic breccias exhibit idiomorphic biotite phenocrysts and plagioclase phenocrysts, with the latter regularly distributed throughout the breccias as porphyritic phenocrysts. The biotite phenocrysts are hypidiomorphic and tabular, partially metasomatized by clay minerals. The plagioclase phenocrysts in the matrix are idiomorphic and partially metasomatized by sericite. The volcanic breccias contain xenomorphic granular quartz grains, which are distributed among felsic spherulites. Besides, xenomorphic opaque minerals are dispersed throughout the matrix (Fig. 3a).

4.1.2. Features of volcanic eruption sequences

The Tunxi Formation is exposed for approximately 5 km across the Tunxi Basin (Fig. 1). The extensive outcrops, especially in the holostratotype, allow for detailed analyses of volcanic sequences and facies. Three eruption sequences were identified in the holostratotype in this study (Fig. 7; Table 2). The first sequence at the bottom is composed of grayish-green crystal tuffs and purplish-gray dacitic tufflavas (the 1st and 2nd layers), with a total thickness of 34.1 m. The rock types and

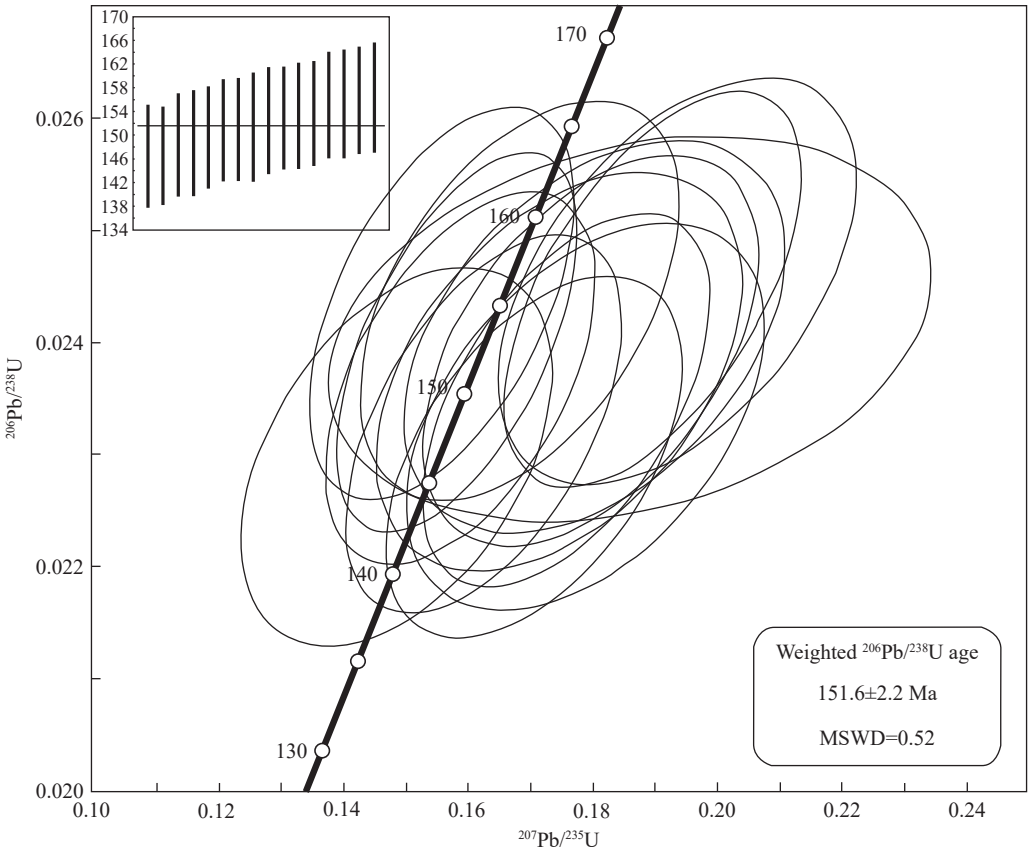

Fig. 7. Concordia diagrams of zircon U-Pb isotopes in the Tunxi Formation at Sanchong Village, Tunxi area, Huangshan City.

thickness of this sequence suggest the initially low eruption intensity of the Tunxi Formation. The second sequence consists of grayish rhyolitic crystal tuffs and grayish-purple rhyolitic tufflavas (the 3rd and 4th layers), with a total thickness of 47.1 m, suggesting slightly higher eruption intensity with a relatively short intermission. The third sequence at the top comprises grayish-purple volcanic breccias, purple dacitic tuffs, and rhyolitic tufflavas (the 5th to 12th layers), with a total thickness of 163.8 m, signaling that the total volcanic activity peaked during the Late Jurassic in the study area. Additionally, the third sequence displays dacitic to rhyolitic magmas, with each sequence beginning with pyroclastic eruption and ending with lava eruption. The gradually increasing thicknesses from the first to the third sequence hint at the progressively elevated eruption intensity. Overall, the three sequences in the Tunxi Formation reflect the complete magmatic process in the study area.

4.2. Geochemistry

4.2.1. Characteristics of major elements

The results of major and trace elements are shown in Table 3. The samples contained 73.11–74.81 wt% of SiO_2, 13.44–14.98 wt% of Al_2O_3, and 6.45–8.18 wt% of total Na_2O and K_2O, with Na_2O/K_2O ratios exceeding 1, indicating potassium enrichment. The total alkali-silica (TAS) diagram (Fig. 8) shows that all samples fell in the zone of calc-alkaline series. Samples belonging to the high-K calc-alkaline series can be observed in the SiO_2-K_2O diagram (Fig. 8).

The Harker diagrams (Fig. 9) illustrate significant linear correlations between the SiO_2 content and the contents of other oxides (e.g., TiO_2, Al_2O_3, Na_2O, and MgO) in the samples. With an increase in the SiO_2 content, the contents of $Fe_2O_3^T$, TiO_2, Al_2O_3, Na_2O, MgO, and Y decreased gradually, suggesting negative correlations.

The region in yellow represents the data of granodiorites from Taiping, Beikaojian, and Dongyuan (Xue HM et al., 2009; Zhou Q et al., 2012; Li PJ et al., 2013), and the region in blue represents the data of granites from Yellow Mountain, Jiuhua Mountain, and Guniujiang (Qiu RL, 1998; Xue HM et al., 2009; Zhang S and Zhang ZC, 2010; Xie JC et al., 2012).

4.2.2. Characteristics of trace elements

All samples were enriched in light rare earth elements (LREEs) compared to heavy rare earth elements (HREEs; Fig. 10a). Their total REE content ranged from 72×10^{-6} to 198×10^{-6}, with an average of 137×10^{-6}. Their total trace element content was lower than the average trace element content of the global granite (290×10^{-6}, Taylor SR and McLennan SM, 1985). The samples exhibited LREE/HREE ratios varying from 13.5 to 17.6 and $(La/Yb)_N$ ratios from 23.9 and 48.6, implying significant differentiation between LREEs and HREEs. Compared to the upper and lower crust (Taylor SR and McLennan SM, 1985), the Tunxi Formation is deficient in HREEs and slightly negative Eu anomalies (Fig. 10), which indicate insignificant fractional crystallization of plagioclase but significant separation of heavy rare earth minerals such as garnet (Fig. 10). The primitive mantle-normalized spidergram reveals relatively high contents of large-ion lithophile elements (LILEs) like Rb, Ba, Th, La, Nd, K but low Sr content. The samples exhibited the loss of high field strength elements (HFSEs) such as Nb, Ta, P, and Ti, resembling arc magmas (Chen XF et al., 2013). The samples displayed Sr and Y content ranges of $(182–300) \times 10^{-6}$ (average: 240×10^{-6}) and $(8.3–15.5) \times 10^{-6}$ (average: 9.9×10^{-6}), respectively, suggesting a high-Sr and low-Y tendency. They fell outside of the adakite zone in the Sr/Y-Y diagram (Fig. 10). Generally, the Tunxi Formation exhibit trace element characteristics similar to the Jiuhua and Yellow mountains. These results prove that the trace elements in the Tunxi Formation vary significantly, exhibiting a minimal association with the fractional crystallization of magmas in the study area.

The (Y+Nb) - Rb and Yb - Ta diagrams (Pearce JA et al., 1984) show that all volcanic rock samples fell within the volcanic arc zone near the transition zone (Fig. 11). This finding implies that the Tunxi Formation shares similar

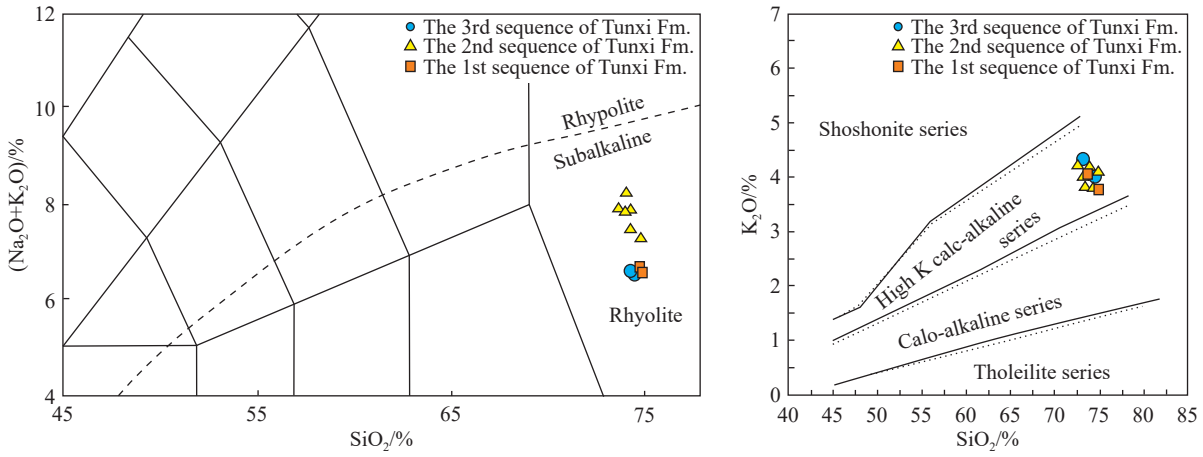

Fig. 8. TAS and SiO_2-K_2O diagrams of Sanchong Village and Huangkou, Tunxi area, Huangshan City (TAS diagram from Middlemost EAK, 1994, with the dashed lines refer to Pceccerillo A and Taylor SR, 1976. In the SiO_2-K_2O diagram, solid lines refer to Peccerillo A and Taylor SR, 1976, and the dashed lines refer to Middlemost EAK, 1985). Fm.–Formation.

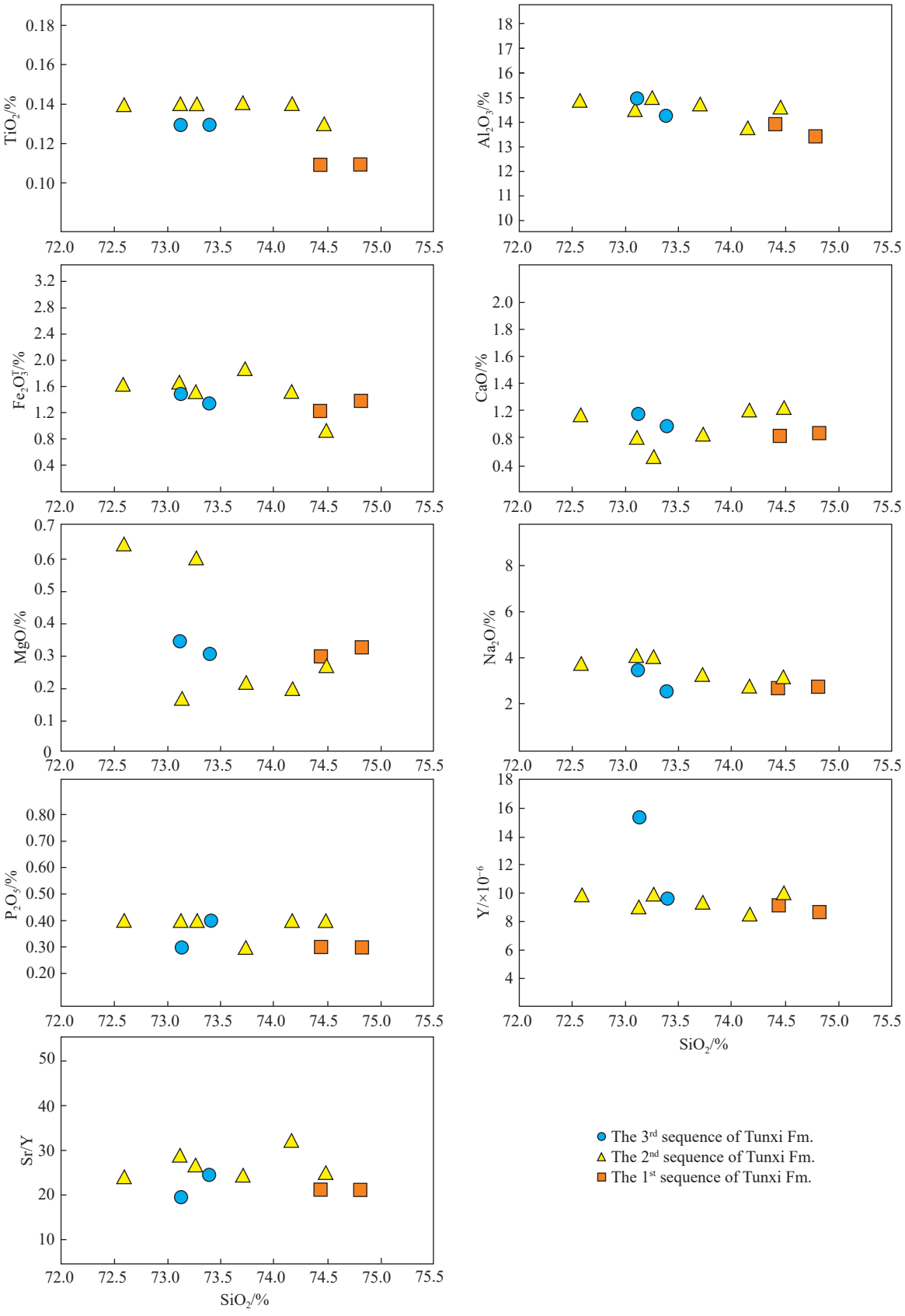

Fig. 9. Harker diagrams of the Tunxi Formation at Sanchong Village and Huangkou, Tunxi area, Huangshan City (after Middlemost EAK, 1994). Fm.–Formation.

geochemical features with volcanic arcs and that its formation is significantly associated with the tectonic activity in the study area. Besides, it might partially relate to the subduction of the oceanic plateaus.

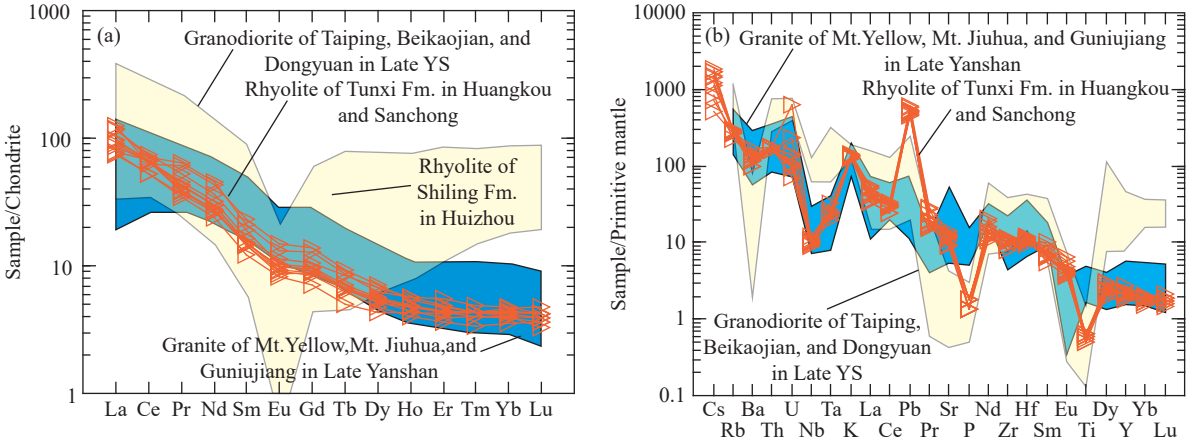

Fig. 10. Chondrite-normalized REE pattern (a) and upper continental crust (UCC)-normalized trace element spider diagram (b) (chondrite data from Boynton WV, 1984, and UCC data from Sun SS and McDonough WF, 1989).

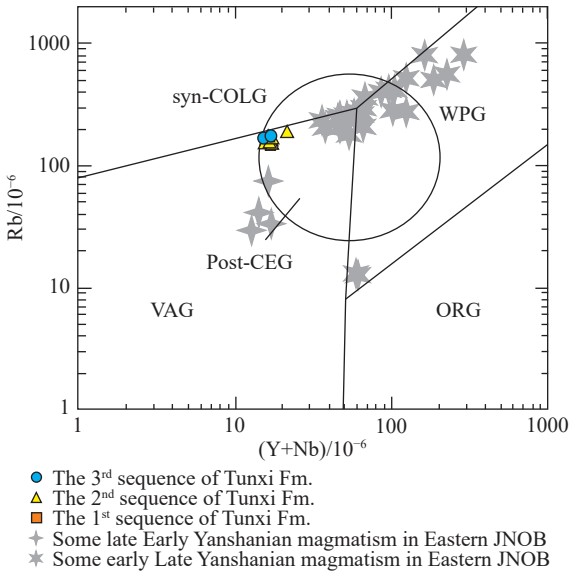

Fig. 11. Y+Nb *vs.* Rb diagram (a) and Yb *vs.* Ta diagram (b) of the Tunxi Formation at Sanchong and Huangkou villages, Tunxi area, Huangshan City (after Pearce JA et al., 1984; granites formed post-collisional extension (post-CEG) after Foster HJ et al., 1997). Fm.–Formation; JNO–Jiangnan orogen.

4.3. Isotopes

Lu-Hf isotope analyses were conducted on zircon grains in 18 samples, namely WN12-T-04, -06, -08, -12, -14, -18, -19, -26, -30, -32, -34, and -49 and P3-TW01 to -TW06. These zircon grains were all dated using the LA-ICP-MS U-Pb dating method (Table 2 and Fig. 12). The analytical results indicate $^{176}Yb/^{177}Hf$ ratios ranging from 0.027984 to 0.047585 and $^{176}Lu/^{177}Hf$ ratios from 0.00117 to 0.001885 (below 0.283). Therefore, the $^{176}Hf/^{177}Hf$ ratios could represent those during the zircon formation. Additionally, the analytical results yielded $\varepsilon_{Hf}(t)$ values ranging from −10.6 to −0.49 (below zero) and the T_{DM2} values from 1875.0 to 1229.5 Ma.

4.4. Zircon U-Pb dating

Zircons in sample series WN12-T from the Tunxi Formation in Sanchong Village (Table 3) were mostly idiomorphic and short prismatic, with grain sizes ranging from 40 μm to 110 μm and length/width ratios from 2∶1 to 3∶1. CL images reveal that these zircons exhibited many bands of zonation (Fig. 6). The U and Th contents in the zircons varied from 527 × 10^{-6} to 1510 × 10^{-6} and from 189 × 10^{-6} to 1055 × 10^{-6}, respectively, with Th/U ratios ranging from 0.36 to 0.70. The zircon grains in the samples yielded U-Pb ages of 151.6 ± 2.2 Ma (n = 16, MSWD = 0.52; Fig. 7). Both CL images and Th/U ratios (> 0.4) suggest the best age estimates of metamorphic zircons.

5. Discussion

5.1. Timing of the volcanism in the Tunxi Basin

The Tunxi Formation is well-developed in the Tunxi Basin. The geochronological data of this formation obtained in this study are shown in Fig. 2 and Table 2. The crystal tuff and tufflava samples from the lower and upper portions of the Tunxi Formation at Huangkou Village yielded ages of 155.8 ± 1.2 Ma and 149.9 ± 2.7 Ma (Ren XX et al., 2015; Tang S et al., 2016), respectively. The rhyolitic samples from the lower portion of the Tunxi Formation at Sanchong Village exhibited ages of 151.6 ± 2.2 Ma. Therefore, the Tunxi Formation in the study area was dated at 156–150 Ma in this study, suggesting that this volcanic unit is the product of the Late Jurassic magmatism.

Many high-precision isotopic ages have been obtained in the study area (Ren XX et al., 2015; Tang S et al., 2016; Yu XQ et al., 2016). The Tunxi Formation in the study area was dated to 156–150 Ma, suggesting the Kimmeridgian to Tithonian stages (Ren XX et al., 2015; Tang S et al., 2016; Yu XQ et al., 2016). Based on recent research on the distributions and types of volcanic rocks, as well as the regional tectonic location (e.g., Han YY et al., 2019), the Mesozoic magmatic activity of the Jiangnan orogen can be divided into two stages: the first stage from 180 Ma to 137 Ma and the second stage from 136 Ma to 120 Ma. Among these, the first stage involved Dongyuan and Zhanggongshan (southern Anhui

Table 2. Zircon Hf isotopic compositions of lavas in the Tunxi Formation.

No.	Sample No.	*t*/Ma	$^{176}Hf/^{177}Hf$	2δ	$^{176}Yb/^{177}Hf$	2δ	$\varepsilon_{Hf}(0)$	$\varepsilon_{Hf}(t)$	t_{DM1}/Ma	t_{DM2}/Ma	$f_{Lu/Hf}$
1	WN12-T-04	146	0.282671	0.000020	0.027984	0.000106	−3.581234	−0.490639	827.03	1229.50	−0.96
2	WN12-T-06	151	0.282651	0.000012	0.030395	0.000301	−4.283737	−1.093435	856.73	1271.68	−0.96
3	WN12-T-08	151	0.282568	0.000012	0.029393	0.000359	−7.197149	−4.003164	972.26	1456.77	−0.96
4	WN12-T-12	156	0.282577	0.000015	0.033963	0.000437	−6.884254	−3.604677	964.85	1435.18	−0.96
5	WN12-T-14	170	0.282596	0.000007	0.037295	0.000255	−6.220471	−2.657128	940.71	1385.53	−0.96
6	WN12-T-18	154	0.282640	0.000026	0.042788	0.000707	−4.680484	−1.474030	883.58	1298.09	−0.96
7	WN12-T-19	152	0.282633	0.000005	0.032116	0.000135	−4.910550	−1.707860	883.88	1311.53	−0.96
8	WN12-T-26	151	0.282620	0.000012	0.030248	0.000176	−5.386960	−2.197644	901.12	1341.96	−0.96
9	WN12-T-30	154	0.282519	0.000013	0.047585	0.000295	−8.941660	−5.754938	1061.44	1570.05	−0.94
10	WN12-T-32	156	0.282601	0.000018	0.029816	0.000395	−6.038756	−2.740893	926.53	1380.31	−0.96
11	WN12-T-34	155	0.282555	0.000036	0.036206	0.000442	−7.675525	−4.425693	998.84	1486.56	−0.96
12	WN12-T-49	149	0.282383	0.000027	0.037112	0.000947	−13.74695	−10.62723	1243.44	1874.99	−0.95
13	P3-TW01	151	0.282332	0.000007	0.033937	0.000775	−9.131060	−5.955741	1054.59	1580.69	−0.96
14	P3-TW02	146	0.282657	0.000007	0.040352	0.000211	−4.068646	−1.023274	857.39	1263.33	−0.95
15	P3-TW03	149	0.282614	0.000004	0.029017	0.000202	−5.571060	−2.418080	907.01	1354.48	−0.96
16	P3-TW04	148	0.282523	0.000027	0.035563	0.000213	−8.820379	−5.722550	1046.24	1563.59	−0.95
17	P3-TW05	155	0.282481	0.000051	0.037980	0.000670	−10.30663	−7.064350	1106.59	1653.95	−0.95
18	P3-TW06	158	0.282569	0.000018	0.033888	0.000388	−7.188859	−3.865277	976.60	1453.26	−0.96

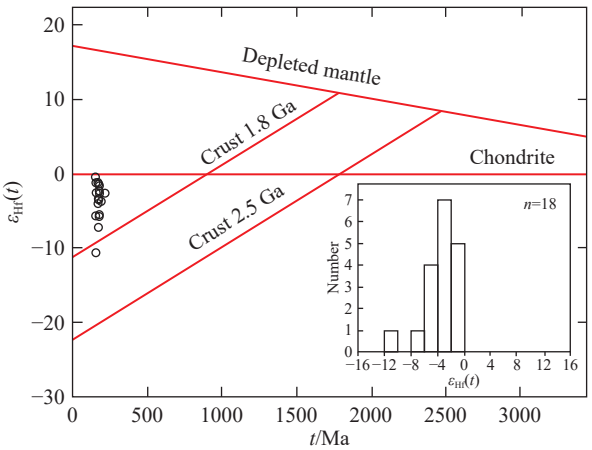

Fig. 12. $\varepsilon_{Hf}(t)$ diagram of zircons in rhyolite in the Tunxi Formation.

Province), Yinshan and Tongchang (Jiangxi Province), and Jiaokengkou and Kailingjiao (Zhejiang Province) (e.g., Yang QK et al., 2019), while the second stage affected Sanqingshan (Jiangxi Province), Anji and Tongshan (Zhejiang Province), Fuling, Shiling, and Qingliangfeng (Anhui Province) (e.g., Han YY et al., 2019). The Tunxi Formation originated from the first stage of magmatic activity.

5.2. Petrogenesis

The Tunxi Formation, an Upper Jurassic volcanic unit in the study area, consists primarily of rhyolitic rocks (SiO_2 > 72.58%), with high alumina content (13.76%–14.98%). This indicates that crustal magmas played a predominant role in the formation of this volcanic unit. The magmas experienced partial melting, with a SiO_2 content ranging from 72.58 to 74.81 wt% and La/Zr, Ce/Zr, and Nb/Zr ratios from 0.21 to 0.48, 0.45 to 0.70, and 0.07 to 0.10, respectively. Therefore, this study posits that the volcanics in the Tunxi Formation originated from upper crustal melting and experienced the fractional crystallization of minerals. The Harker diagrams (Fig. 9) show that with an increase in the SiO_2 content, the weight percentages of TiO_2, Al_2O_3, $Fe_2O_3^T$, MgO, and Na_2O decrease, accounting for the evolutionary trend of crystallization differentiation. In contrast, the P_2O_5 content is stable or even slightly increases, potentially suggesting the mixing of minor quantities of foreign substances rather than pure crystallization differentiation in the evolutionary stage of high-content Si. This is similar to the evolution of assimilation-fractional crystallization (AFC) and hybridization. The magmatic rocks in the Tunxi Formation primarily underwent the crystallization differentiation of plagioclase and amphibole in the early stage of this formation and were mixed with surrounding rocks in its late stages. The Tunxi Formation exhibits high SiO_2 content (about 72.6% to 74.8%), Sr-Nd-Hf enrichment in isotopic composition, LILE enrichment, and HFSE depletion, indicating that the magmas were primarily sourced from the crust.

Thrust nappes serve as an important criterion for discriminating extrusion in a tectonic setting. During the Early Yanshanian (Wang TF, 2012), many thrust nappe structures were formed in the study area (Fig. 13). For instance, klippes and tectonic windows are found at Xiaoxi Village, Shexian County, Huangshan City, overlain by the Hongqin Formation (Xu XB et al., 2016). Thrust nappe structures can be observed at the expressway entrance of Shexian County, with the underlying epimetamorphic rocks directly thrust onto the Hongqin Formation (Fig. 13a). Therefore, the potential collisional event during the late Middle Jurassic (Early Yanshanian) might have occurred in the study area. The Y+Nb *vs.* Rb and Yb *vs.* Ta diagrams (Pearce JA et al., 1984) of the Tunxi Formation correspond to the former hypothesis (Fig. 11). According to these diagrams, the origin of the magmas is associated with the collision of oceanic blocks, which interacted with the tectonic setting of the study area

Table 3. LA-ICP-MS zircon U–Pb dating of the Tunxi Formation.

Samples	Th/×10^{-6}	U/×10^{-6}	Th/U	Ratio of isotope						Age/Ma			
				$^{207}Pb/^{206}Pb$	1σ	$^{207}Pb/^{235}U$	1σ	$^{206}Pb/^{238}U$	1σ	$^{207}Pb/^{235}U$	1σ	$^{206}Pb/^{238}U$	1σ
WN12-T-04	310	563	0.55	0.0465	0.0032	0.1485	0.0102	0.0007	0.4385	141	9.0	146	4.3
WN12-T-03	379	841	0.45	0.0532	0.0031	0.1706	0.0097	0.0007	0.5037	160	8.4	146	4.2
WN12-T-33	378	846	0.45	0.0499	0.0029	0.1625	0.0090	0.0007	0.5321	153	7.9	148	4.3
WN12-T-16	391	778	0.50	0.0553	0.0037	0.1787	0.0117	0.0007	0.4599	167	10.1	149	4.4
WN12-T-17	722	1283	0.56	0.0540	0.0030	0.1757	0.0094	0.0007	0.5402	164	8.1	150	4.3
WN12-T-08	545	982	0.55	0.0482	0.0027	0.1587	0.0089	0.0007	0.5127	150	7.8	151	4.3
WN12-T-06	1055	1510	0.70	0.0484	0.0026	0.1584	0.0083	0.0007	0.5561	149	7.3	151	4.4
WN12-T-26	235	606	0.39	0.0529	0.0036	0.1746	0.0120	0.0007	0.4448	163	10.4	151	4.6
WN12-T-19	189	527	0.36	0.0540	0.0035	0.1796	0.0110	0.0007	0.4865	168	9.5	152	4.5
WN12-T-42	680	1071	0.64	0.0477	0.0025	0.1582	0.0079	0.0007	0.5780	149	6.9	153	4.4
WN12-T-13	319	710	0.45	0.0539	0.0037	0.1802	0.0125	0.0007	0.4296	168	10.8	153	4.5
WN12-T-30	657	1393	0.47	0.0555	0.0063	0.1859	0.0198	0.0007	0.2735	173	16.9	154	4.4
WN12-T-34	475	862	0.56	0.0458	0.0026	0.1557	0.0087	0.0007	0.5277	147	7.6	155	4.5
WN12-T-41	289	862	0.46	0.0498	0.0032	0.1683	0.0105	0.0007	0.4808	158	9.1	155	4.6
WN12-T-32	491	977	0.50	0.0555	0.0029	0.1896	0.0097	0.0007	0.5746	176	8.3	156	4.5
WN12-T-12	261	581	0.45	0.0574	0.0036	0.1935	0.0117	0.0007	0.4975	180	10.0	156	4.7

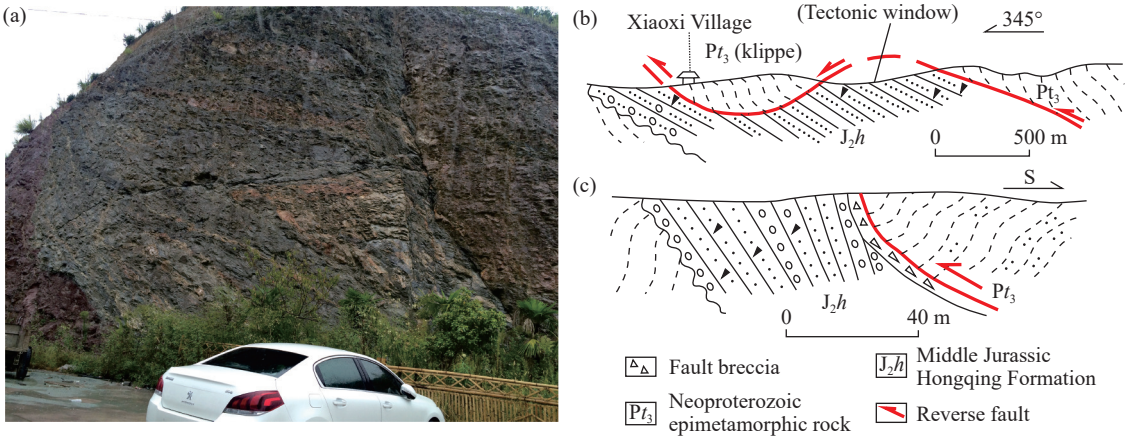

Fig. 13. Nappe structures in the study area. a–nappe structure at the highway entrance of Shexian County; b–tectonic window at Xiaoxi Village, Shexian County; c–nappe structure at Jinzhu Village, Xiuning County (b and c modified from Yu XQ et al., 2006).

during that collision. Liegeois JP et al. (1998) considered that the presence of high-K alkaline magmas signals orogeny and the geochemistry of igneous rocks in a low-Sr and low-Yb zone. Samples in the diagrams resemble the Himalayan granites, with the crust thickness at the end of the orogenic period slightly larger than the normal thickness proposed inaugurally by Zhang Q et al. (1998). The Tunxi Formation exhibits $\varepsilon_{Hf}(t)$ and T_{DM2} values ranging from −10.6 to −0.49 and from 1875.0 Ma to 1229.5 Ma, respectively, indicating that this formation originated primarily from the remnants of the ancient crust and partial melting from the Paleo- to the Neoproterozoic (Fig. 12).

The magmatic ages of the Late Mesozoic volcanic basins in the Jiangnan orogen reveal that unique magmatic activity and mineralization occurred in the eastern Jiangnan orogen from 150 Ma to 140 Ma (e.g., Chen XF et al., 2013; Zhou J et al., 2014). In contrast, volcanic rocks were absent in the western Jiangnan orogen during the same period. To account for these phenomena, this study proposed a model to illustrate the subduction process of the paleo-Pacific plate (Fig. 14). The different age ranges of the volcanic units in the volcanic basins within the Jiangnan orogen indicate varying degrees of the influence of the subduction. With an increase in the slab density at 150 Ma, the paleo-Pacific plate was further subducted throughout the Jiangnan orogen. Accordingly, vast intrusions were formed in the eastern and western parts of the Jiangnan orogen, whereas the volcanic rocks (the Tunxi Formation) only erupted in the eastern Jiangnan orogen (Fig. 14b). These indicate that the eruption intensity was relatively strong in the eastern Jiangnan orogen, leading to regional large-scale volcanism. From 150 Ma to 140 Ma, magmatism occurred along the eastern Jiangnan orogen, suggesting that the magmas still intensified. Moreover, some changes in the geochemical features of elements within the magmas, such as high $\varepsilon_{Nd}(t)$ and $\varepsilon_{Hf}(t)$ values (e.g., Zhou J et al., 2014) and the shift of granitic magmas from I-type to S-type and then to A-type (Lü JS et al., 2017), indicate increased mantle-derived materials and enhanced magmatic activity during this period. These pieces of evidence suggest that the paleo-Pacific plate began to retreat from the eastern Jiangnan orogen because of

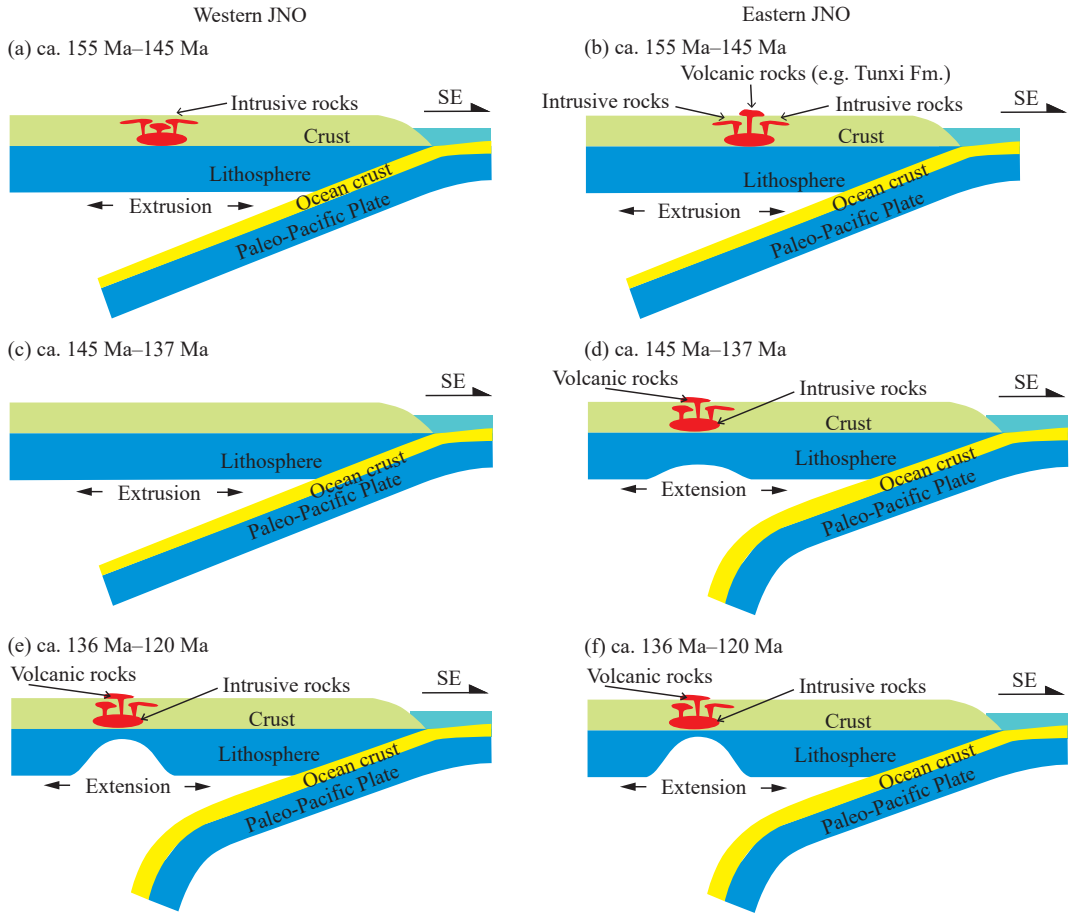

Fig. 14. Tectonic model showing the tectono-magmatic evolution of the Jiangnan orogen from 160 Ma to 140 Ma. Fm.–Formation; JNO–Jiangnan orogen.

the increased in-slab density (Fig. 14d). However, the paleo-Pacific plate did not noticeably retreat in the western Jiangnan orogen due to subtle magmatism (Fig. 14c).

In sum, the Tunxi Formation might have been formed in the compressional orogenic stage that spanned from 154.7 ± 2.5 Ma to 149.9 ± 2.7 Ma. The Early Yanshanian magmatic activity might have been caused by the subduction of the northwestern Izanagi block (e.g., Isozaki Y et al., 2010). The magmas, comprising primarily granodiorites, are potentially associated with the northwestward subduction of the paleo-Pacific plate during the Late Jurassic. The magmatic activity in the Jiangnan orogen might have begun earlier in its eastern proportion from 150 Ma to 140 Ma.

5.3. Geological implications for the evolution of Mamenchisauridae in eastern China

The regional chronological study of the authors suggests that the bottom of the Tunxi Formation has an age of 156 Ma or above. Additionally, the Tunxi Formation shows an unconformable contact with the underlying Hongqin Formation, with the fossil-bearing horizon located in the middle part of the Hongqin Formation. Therefore, the two mamenchisaurid genera *Huangshanlong anhuiensis* and *Anhuilong diboensis* found at this horizon may have ages spanning from the middle to late Middle Jurassic. Given that most Middle Jurassic sauropods in China, especially the dominant *Omeisaurus* spp., were reported in the Lower Shaximiao Formation, southwestern China (e.g., Young CC, 1939 and 1958; Dong ZM and Tang ZL, 1984; Ouyang H, 1989; Jiang S et al., 2011; Xing LD et al., 2015; Ren XX et al., 2022, 2023), the two mamenchisaurid genera in eastern China possibly share similar ages with the *Omeisaurus* spp. (Bajocian to Bathonian; Ren XX et al., 2022, 2023). Besides, a phylogenetic study has confirmed that the two sauropod genera found in Anhui are sister taxa, as members of Mamenchisauridae. They are more closely related to *Omeisaurus* than to the clade including all other mamenchisaurids (Ren XX et al., 2018). This verified the aforementioned age hypothesis that these two Anhui mamenchisaurid genera share generally similar ages with the *Omeisaurus* spp. and other relative Middle Jurassic mamenchisaurids in China. This also indicates that the two mamenchisaurid taxa are possibly part of the evolutionary radiation of Middle Jurassic mamenchisaurids in southwestern China (Fig. 15).

However, this is not the case for the distribution of Late Jurassic mamenchisaurid lineage in China (Fig. 16). During the Late Jurassic, mamenchisaurids further predominated in East Asia, where *Mamenchisaurus* spp. was the major genus of this lineage. Currently, the only reports on the Late Jurassic non-mamenchisaurids in China include *Bellusaurus sui* and

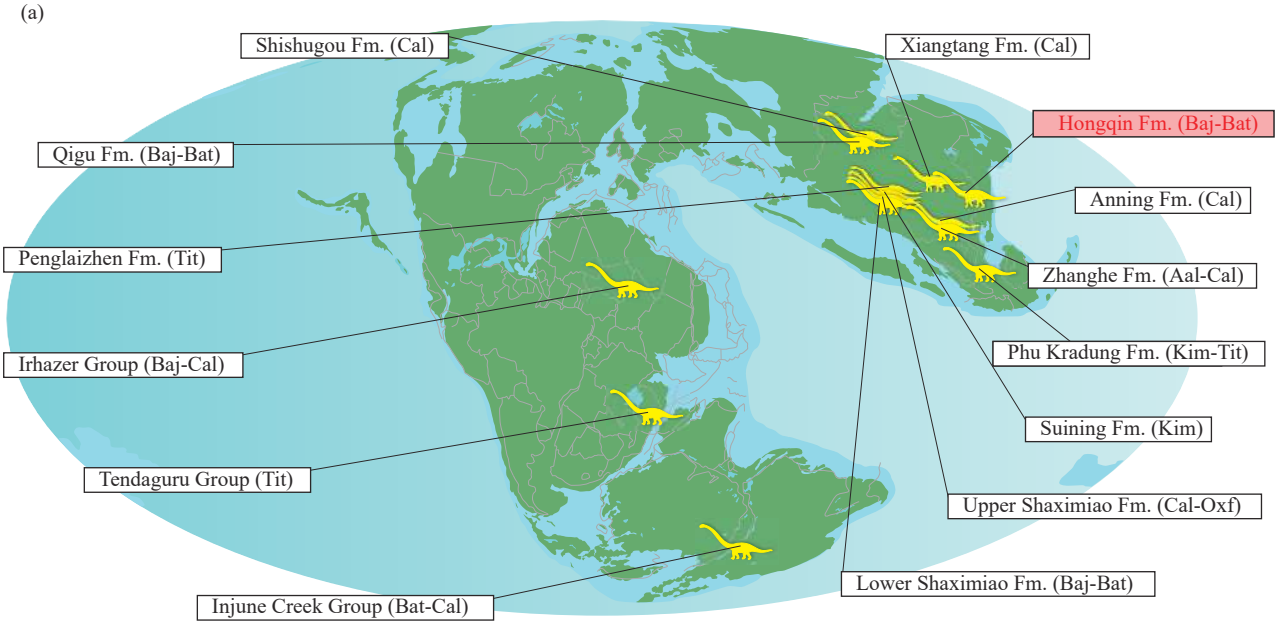

(b)

Region		Sichuan		Yunnan (Yuanmou)	Yunnan (Lufeng)	Anhui	Gansu	Xinjiang	Thailand	Niger	Australia	Tanzania
Late Jurassic	Tithonian	PLZ Fm.	①		AN Fm.	⑭ TX Fm.						T Fm. ㉙
	Kimmeridgian	SN Fm.	②	TD Fm.	MDS Fm.			KLZ Fm.	PK Fm. ㉖		IC Group	
	Oxfordian	USXM Fm.	③④⑤⑥	SD Fm.	LLC Fm.		⑲ XT Fm.	⑳㉑㉒㉓㉔ SSG Fm.		Irhazer Group		
Middle Jurassic	Callovian			ZH Fm.			HG Fm.				㉘	
	Bathonian	LSXM Fm.	⑦⑧⑨⑩⑪	⑫⑬	⑮⑯ CJ Fm.	⑰ HQ Fm.		QG Fm. ㉕		㉗	Hutton Ss.	
	Bajocian					⑱	YJ Fm.					
	Aalenian	XTG Fm.						XSY Fm.				

Fig. 15. Paleogeographic reconstruction (a) and stratigraphic correlation (b) of the primary Middle to Late Jurassic mamenchisaurid faunas. Paleogeographic reconstruction of 170 Ma using PALEOMAP. Mamenchisaurids (1–29): *Mamenchisaurus anyuensis*; *Qijianglong guokr*; *M. constructs*; *M. hochuanensis*; *M. youngi*; *M. jingyanensis*; *Omeisaurus tianfuensis*; *O. jiaoi*; *O. luoquanensis*; *O. maoi*; *Abrosaurus dongpoi*; *Yuanmousaurus jiangyiensis*; *Eomamenchisaurus yuanmouensis*; *M. yunnanensis*; *Analong chuanjieensis*; *Chuanjiesaurus anaensis*; *Huangshanlong anhuiensis*; *Anhuilong diboensis*; *M. hochuanensis*; *Tienshanosaurus chitaiensis*; *M. sinocanadorum*; *Bellusaurus sui*; *Klamelisaurus gobiensis*; *Rhomaleopakhus turpanensis*; *Xinjiangtitan shanshanesis*; *M.* sp.; *Spinophorosaurus nigerensis*; *Rhoetosaurus brownei*; *Wamweracaudia keranjei*. Aal–Aalenian; AN–Anning; Baj–Bajocian; Bat–Bathonian; Cal–Callovian; CJ–Chuanjie; Fm. –Formation; HG–Honggou; HQ–Hongqi; IC–Injune Creek; Kim–Kimmeridgian; KLZ–Kalazi; LLC–Laoluocun; LSXM–Lower Shaximiao; MDS–Madishan; Oxf–Oxfordian; PLZ–Penglaizhen; PK–Phu Kradung; SD–Shedian; SN–Suining; Ss–Sandstone; SSG–Shishugou; T–Tendaguru; TD–Tuodian; Tit–Tithonian; TX–Tunxi; USXM–Upper Shaximiao; XT–Xiangtang; XTG–Xintiangou; YJ–Yaojie; ZH–Zhanghe.

Fushanosaurus qitaiensis from the Shishugou Formation in Xinjiang and *Daanosaurus zhangi* from the Upper Shaximiao Formation in Sichuan (e.g., Dong ZM, 1990). A recent phylogenetic study indicates that *Bellusaurus sui* and *Daanosaurus zhangi* might be the putative juvenile mamenchisaurids (Moore AJ et al., 2023). However, these discoveries are isolated, with no other sauropod fossils excavated in the quarries. In contrast, within the quarries bearing fossils of the Middle Jurassic dinosaurs, many neosauropods, along with diverging non-neosauropodan eusauropods, were discovered at the same horizon, possibly reflecting great differentiation in habitats and niches (Ren XX et al., 2023). In comparison, no coexisting sauropod lineage has been reported in the Late Jurassic quarries in China. Besides, most of the Late Jurassic sauropod fossil-bearing horizons are dominated by the elements of mamenchisaurids.

Current evidence suggests that the lower diversity of the Late Jurassic eusauropod taxa in East Asia might be due to fewer fossiliferous terrestrial horizons compared to the Middle Jurassic (Xing LD et al., 2015). The fragmentation of

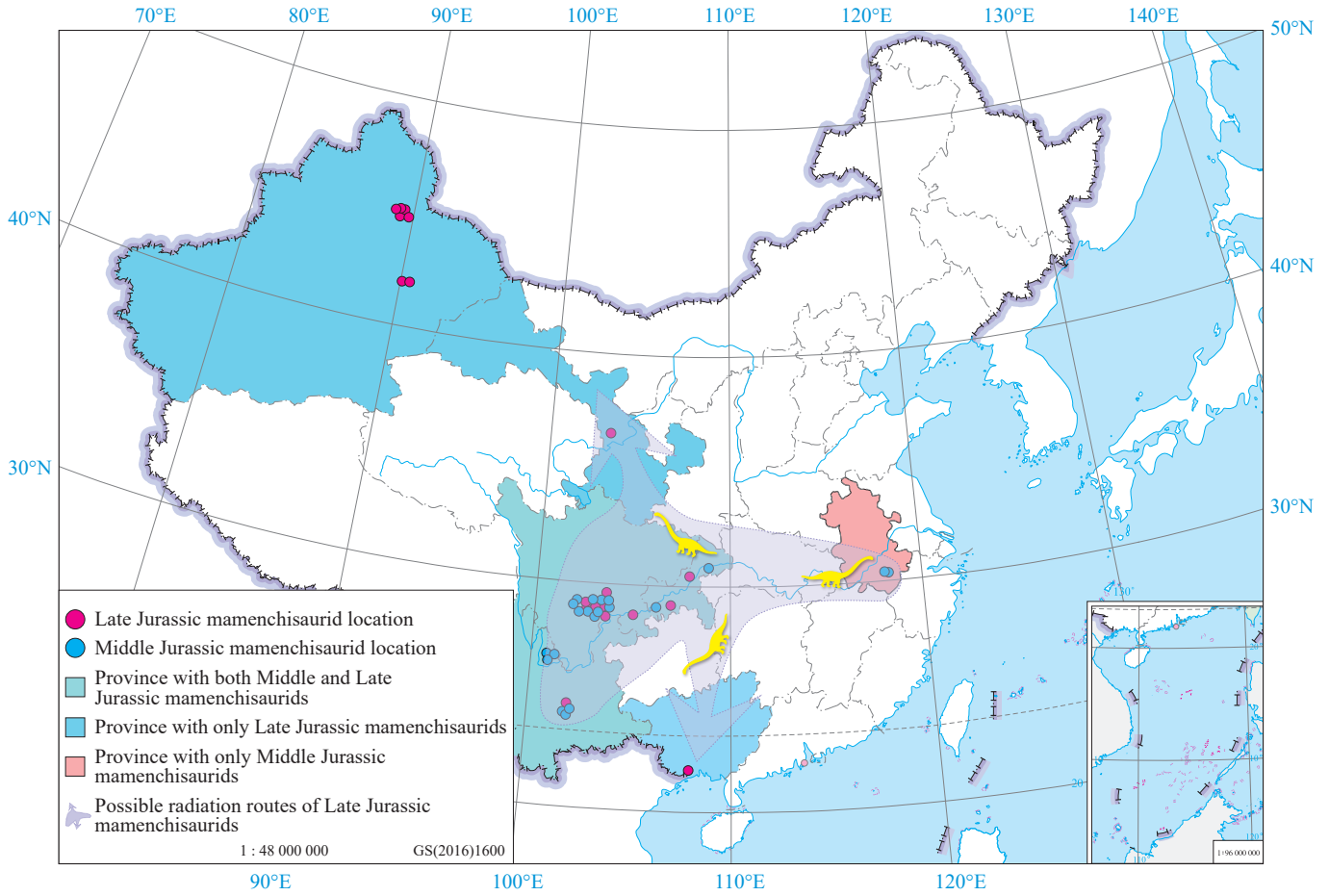

Fig. 16. Localities of main valid mamenchisaurid dinosaurs in China.

supercontinent Pangea from the Middle to Late Jurassic (e.g., Mannion PD et al., 2019) may have further enhanced the specialization and predominance of this endemic sauropod fauna in East Asia during the Late Jurassic. Finally, this sauropod fauna was replaced by titanosauriform eusauropods across the Jurassic-Cretaceous boundary. To date, all the fossil records discovered in East Asia are located at the horizons in the western part, including the Upper Shaximiao, Suining, and Penglaizhen formations in Sichuan and Chongqing (e.g., Young CC and Chao ZK, 1972; Ye Y et al., 2001; Xing LD et al., 2015; Peng GZ et al., 2019), the Anning Formation in Yunnan (Fang XS et al., 2004), the Xiangtang Formation in Gansu (Young CC, 1958), the Shishugou and Kalazha formations in Xinjiang (e.g., Moore AJ et al., 2023), and the Phu Kradung Formation in Thailand (Suteethorn S et al., 2013). The environmental shift (e.g., the Late Jurassic global aridification events) likely further consolidated the ecological niches of regionally dominant species. Furthermore, current phylogenetic analyses show that the two eastern Middle Jurassic mamenchisaurids share close relationships wiht other Late Jurassic East Asian mamenchisaurids. Consequently, Middle Jurassic mamenchisaurids underwent further radiation during the Late Jurasic, though their distributional expansion predominantly shifted toward northwestern and southern regions. Notably, Late Jurassic strata in eastern China completely lack the reports of mamenchisaurids.

Therefore, this study proposes that during the Late Jurassic, the subduction of the paleo-Pacific plate triggered multiple large-scale volcanic eruptions and subsequent intrusions in eastern China (the Tunxi Formation represents these volcanic activities in the eastern Jiangnan orogen). This intense tectonic transformation likely caused substantial or abrupt environmental changes in the Upper Jurassic terrestrial basins of eastern China, significantly impacting the potential evolutionary radiation of Late Jurassic mamenchisaurids. Additionally, the subduction process stimulated the development of major depositional discontinuities in Late Jurassic terrestrial basins of eastern China, which may have erased the potential sedimentary fossil records of Late Jurassic mamenchisaurids.

6. Conclusions

During the Middle to Late Jurassic period, volcanic activities in South China belong to the transitional phase from the peak of subduction compression to post-subduction extension in continental margin arcs. During this period, magmatism and mineralization in the Jiangnan orogen primarily occurred in its eastern segment (e.g., Tunxi Formation), synchronously with volcanic activities in southeastern China, dating between 165–145 Ma.

Concurrently, intense intrusive activities occurred, which differed from the widely distributed bimodal volcanic rocks of the Late Mesozoic era, representing products drom distinct regions and tectonic stages. Between 155–145 Ma, magmatic activites persisted in the eastern segment of the Jiangnan orogen. After 145 Ma, geochemical signatures indicate increased mantle-derived material and enhanced magmatism. These findings suggest that due to increased intra-late density, the paleo-Pacific plate began to retreat from the eastern segment of the Jiangnan orogen, while its western segment showed no significant retreat due to weak magmatic activity.

Petrological studies have identified three eruptive sequences in the type section of Tunxi Formation, all beginning with pyroclastic eruptions and ending with lava flows. The final sequence shows a compositional transition from dacitic to rhyolitic volcanic rocks. Major and trace element analyses indicate these volcanic rocks belong to the high-K calc-alkaline series, similar to coeval volcanic rocks in southeastern China. New regional isotopic dating yields an age of 151.6 ± 2.2 Ma (n=16, MSWD=0.52). This result reinforces the established age range of 150 Ma to 156 Ma for the Tunxi Formation, confirming its formation durign the first magmatic episode in the eastern Jiangnan orogenic belt and adjacent areas, while correlating with the second volcanic activity cycle of the Yanshanian orogeny along eastern coastal regions. Zircon Hf isotopic characteristics of the Tunxi Formation are related to the reworking of ancient crustal residues (Meso- to Neoproterozoic). The magmatic activity may be associated with northwestward subudction of the paleo-Pacific plate during the Late Jurassic, partially representing volcanic arc magmatism. Subsequent compressional intrusions in the eastern Jiangnan orogen indicate that between 151 Ma and 140 Ma, the arc environment dominated by paleo-Pacific plate subduction rapidly transitioned into a back-arc extensional setting.

This study provides novel insights into the evolution of basal non-neosauropodan eusauropods in Asia from the Middle to Late Jurassic. The subduction of the paleo-Pacific plate resulted in significant eruptions and subsequent intrusions in eastern China during the Late Jurassic. Such a drastic tectonic transformation could cause a substantial or sudden change in the environments of Late Jurassic terrestrial basins in eastern China, severely affecting the evolutionary radiation of Late Jurassic mamenchisaurids, which restricted the distribution of dinosaurs in eastern China and drove their migration to other regions such as northwestern (Gansu, Xinjiang), southern (Guangxi), and even Southeast Asia (Thailand).

This study represents a successful attempt to investigate the relationships among tectonic-basin evolution, environmental changes, and biological evolution. While the correlations between these phenomena still require further evidence. For further research on the impacts of the Jurassic - Early Cretaceous tectonics, additional data such as paleomagnetic and paleontological datasets are required.

CRediT authorship contribution statement

Xin-Xin Ren wrote the manuscript. Others helped Xin-xin Ren conceive the original idea of this study. El-Wardany RM polished this manuscript.

Declaration of competing interest

The authors declare no conflict of interest.

Acknowledgment

This work was supported by the China Geological Survey (DD20230221), the National Natural Science Foundation of China (42102018), and the Strategic Priority Research Program of the Chinese Academy of Sciences (XDB26000000). The authors would like to express their sincere gratitude to Hai-lu You from the Institute of Vertebrate Paleontology and Paleoanthropology (IVPP), Chinese Academy of Sciences for his early discussion and suggestions. The authors would like to extend their appreciation to Prof. Zhi-guo Bi from the No. 327 Geological Team (AH327), Bureau of Geology and Mineral Exploration of Anhui Province, Prof. Guo-qiang Pan from the Nanjing University (NJU), and Prof. Li-fu Jiang from Anhui Geological Survey (AHGS) for their valuable instructions in early fieldwork. Our thanks also go to Prof. Tian-qiu Hong and Dr. Zi-liang Fan from the Hefei University of Technology (HFUT) for their helpful suggestions on material preparation and to Prof. Wei Li from the Institute of Geology and Geophysics (IGG), Chinese Academy of Science for his important assistance in the Hf isotope dating. Additionally, our sincere appreciation goes to Li-qiong Jia and Zi-guo Hao for their suggestions regarding the improvement of this manuscript and to three anonymous reviewers and editors for their thoughtful reviews.

References

Andersen T. 2002. Correction of common lead in U-Pb analyses that do not report 204Pb. Chemical Geology, 192(1–2), 59–79. doi:10.1016/S0009-2541(02)00195-X.

Boynton WV. 1984. Cosmochemistry of the earth elements: Meteorite studies. Elsevier, 89–92. doi:10.1016/B978-0-444-42148-7.50008-3.

Chen PJ. 2000. Comments on the classification and correlation of non–marine Jurassic and Cretaceous of China. Journal of Stratigraphy, 24, 114–119 (in Chinese with English abstract). doi: 10.1007/s11434-005-0340-5.

Chen XF, Wang YG, Sun WD, Yang XY. 2013. Zircon U-Pb chronology, geochemistry and genesis of the Zhuxiling granite in Ningguo, Southern Anhui. Acta Geologica Sinica, 87(11), 1663–1678 (in Chinese with English abstract). doi: 10.19762/j.cnki.dizhixuebao.2013.11.003.

Chu NC, Taylor RN, Chavagnac V, Nesbitt RW, Boella RM, Milton JA, German CR, Bayon G, Burton K. 2002. Hf isotope ratio analysis using multi-collector inductively coupled plasma mass spectrometry: an evaluation of isobaric interference corrections. Journal of Analytical Atomic Spectrometry, 17, 1567–1574. doi: 10.1039/B206707B.

Dong ZM. 1990. On remains of the sauropods from Kelamaili Region,

Junggar Basin, Xinjiang, China. Vertebrata PalAsiatica, 28(1), 43–58 (in Chinese with English abstract). doi: 10.19615/j.cnki.1000-3118.1990.01.005.

Dong ZM, Tang ZL. 1984. Note on a new Mid-Jurassic sauropod (*Datousaurus bashanensis* gen. et sp. Nov.) form Sichuan Basin, China. Vertebrata PalAsiatica, 22(1), 69–75 (in Chinese with English abstract).

Fang XS, Zhao XJ, Lu LW, Cheng ZW. 2004. Discovery of Late Jurassic Mamenchisaurus in Yunnan, southwestern China. Geological Bulletin of China, 23, 1005–1009 (in Chinese with English abstract). doi: 10.1007/s11670-004-0048-0.

Fisher CM, Vervoort JD, Hanchar JM. 2014. Guidelines for reporting zircon Hf isotopic data by LA-MC-ICPMS and potential pitfalls in the interpretation of these data. Chemical Geology, 363, 125–133. doi: 10.1016/j.chemgeo.2013.10.019.

Foster HJ, Tischendorf G, Trumbull RB. 1997. An evaluation of the R. (Y +Nb) discrimination diagram to infer tectonic setting of silicic igneous rock. Lithos, 40, 261–293. doi: 10.1016/S0024-4937(97)00032-7.

Goto A, Tatsumi Y. 1996. Quantitative analyses of rock samples by an X–ray fluorescence spectrometer (II). Rigaku J, 13, 20–39.

Han YY, Yan J, Yang C, Wang SN. 2019. Zircon age dating and geochronologica framwork of the granites in the Taoling-Duangxin Area, Eastern Jiangnan Orogenic Belt. Mineralogy and Petrology, 39(2), 34–44 (in Chinese with English abstract). doi: 10.19719/j.cnki.1001-6872.2019.02.05.

Huang JD, You HL, Yang JT, Ren XX. 2014. A new sauropod dinosaur from the Middle Jurassic of Huangshan, Anhui Province. Vertebrata Palasiatica, 52, 390–400 (in Chinese with English abstract). doi: 10.19615/j.cnki.1000-3118.2014.04.004.

Iizuka T, Hirata T. 2005. Improvements of precision and accuracy in situ Hf isotope microanalysis of zircon using the laser ablation–MC–ICPMS technique. Chemical Geology, 220, 121–137. doi: 10.1016/j.chemgeo.2005.03.010.

Isozaki Y, Aoki K, Nakama T, Yanai S. 2010. New insight into a subduction–related orogen: A reappraisal of the geotectonic framework and evolution of the Japanese Islands. Gondwana Research, 18, 82–105. doi: 10.1016/j.gr.2010.02.015.

Jiang LL, Hu QZ, Zhu Q, Huang DZ, Wang DE. 2016. Late Mesozoic Multi–stage structural deformations feature in the adjacent region among Anhui, Zhejiang, and Jiangxi Province. Earth Science Frontiers, 23, 137–147 (in Chinese with English abstract). doi: 10.13745/j.esf.2016.04.012.

Jiang S, Li F, Peng GZ, Ye Y. 2011. A new species of Omeisaurus from the Middle Jurassic of Zigong, Sichuan. Vertebrata Palasiatica, 49(2), 185–194 (in Chinese with English abstract). doi: 10.19615/j.cnki.1000-3118.2011.02.004.

Li PJ, Yu XQ, Li HY, Qiu JT, Zhou X. 2013. Jurassic-Cretaceous tectonic evolution of Southeast China: Geochronological and geochemical constraints of Yanshanian granitoids. International Geology Review, 55(10), 1202–1219 (in Chinese with English abstract). doi: 10.1080/00206814.2013.771952.

Liegeois JP, Navez J, Hertogen J, Black R. 1998. Contrasting origin of post–collisional high–K calc–alkaline and shoshonitic versus alkaline and oeralkaline granitoids. The use of sliding normalization. Lithos, 45, 1–28. doi: 10.1016/S0024-4937(98)00023-1.

Liu JX, Wang S, Wang XL, Du DH, Xing GF, Fu JM, Chen X, Sun ZM. 2020. Refining the spatio-temporal distributions of Mesozoic granitoids and volcanic rocks in SE China. Journal of Asian Earth Sciences, 201, 104503. doi: 10.1016/j.jseaes.2020.104503.

Liu Y, Liu XM, Hu ZC, Wu CR, Yuan HL, Gao S. 2007. Evaluation of accuracy and long–term stability of determination of 37 trace elements in geological samples by ICP–MS. Acta Petrologica Sinica, 23, 1203–1210 (in Chinese with English abstract). doi: 10.3321/j.issn:1000-0569.2007.05.034.

Liu YS, Gao S, Hu ZC, Gao CG, Zong KQ, Wang DB. 2010. Continental and Oceanic Crust Recycling–induced Melt–Peridotite Interactions in the Trans–North China Orogen: U–Pb Dating, Hf Isotopes and Trace Elements in Zircons from Mantle Xenoliths. Journal of Petrology, 51, 537–571 (in Chinese with English abstract). doi: 10.1093/petrology/egp082.

Ludwig KR. 2003. User's manual for Isoplot/Ex version 3.00, a geochronological toolkit for Microsoft Excel. Berkeley Geochronology Center Special Publications, California, Berkeley 4, 72.

Lü JS, Zhang XH, Sun JD, Zhang Y, Wu B, Luo XQ. 2017. Spatiotemporal evolution and metallogenic regularity of felsic rocks in the Yanshanian of the eastern segment Qinhang metallogenic belt, South China. Acta Petrologica Sinica, 33(11), 3635–3658 (in Chinese with English abstract).

Middlemost EAK. 1985. Magmas and Magmatic Rocks: An Introduction to Igneous Petrology. London, Longman Group, 1–266. doi: 10.1180/minmag.1986.050.355.34.

Middlemost EAK. 1994. Naming materials in the magma/igneous rock system. Earth–Science Reviews, 37, 215–224. doi: 10.1016/0012-8252(94)90029-9.

Mannion PD, Upchurch P, Schwarz DA, Wings O. 2019. Taxonomic affinities of the putative titanosaurs from the Late Jurassic Tendaguru Formation of Tanzania: phylogenetic and biogeographic implications for eusauropod dinosaur evolution. Zoological Journal of the Linnean Society, 99, 1–126. doi: 10.1093/zoolinnean/zly068.

Moore AJ, Barrett PM, Upchurch P, Liao CC, Ye Y, Hao BQ, Xu X. 2023. Re-assessment of the Late Jurassic eusauropod *Mamenchisaurus sinocanadorum* Russell and Zheng, 1993, and the evolution of exceptionally long necks in mamenchisaurids. Journal of Systematic Palaeontology, 21(1), 2171818. doi: 10.1080/14772019.2023.2171818.

Nowell GM, Kempton PD, Noble SR, Fitton JG, Saunders AD, Mahoney JJ, Taylor RN. 1998. High precision Hf isotope measurements of MORB and OIB by thermal ionization mass spectrometry: Insights into the depleted mantle. Chemical Geology, 149, 211–233. doi: 10.1016/S0009-2541(98)00036-9.

Ouyang H. 1989. A new sauropod from Dashanpu, Zigong Co., Sichuan Province (*Abrosaurus dongpoensis* gen. et sp. nov.). Zigong Dinosaur Museum Newsletter, 2, 10–14 (in Chinese with English abstract).

Paton C, Hellstrom J, Paul B, Woodhead J, Hergt J. 2011. Iolite: Freeware for the visualisation and processing of mass spectrometric data. Journal of Analytical Atomic Spectrometry, 26, 2508–2519. doi: 10.1039/C1JA10172B.

Peccerillo A, Taylor SR. 1976. Geochemistry of eocene calc–alkaline volcanic rocks from the Kastamonu area, northern Turkey. Contributions to Mineralogy and Petrology, 58, 63–81. doi: 10.1007/BF00384745.

Pearce JA, Harris NBW, Tindle AG. 1984. Trace element discrimination diagrams for the tectonic interpretation of granitic rocks. Journal of petrology, 25, 956–983. doi: 10.1093/petrology/25.4.956.

Peng GZ, Qin G, Ye Y, Zhu TX, Hao BQ, Jiang S, Tang W, Li SJ. 2019. Discovery and research of dinosaur fossils in Sichuan. Acta of Sichuan Geology, 39(2), 215–223 (in Chinese with English abstract).

Qiu RL. 1998. Magmatic differentiation and genesis of Jiuhuashan granite. Acta Petrologica et Mineralogica, 17(4), 308–315 (in Chinese with English abstract).

Ren XX, Huang JD, Hong TQ, Bi ZG. 2017. New research progress in Jurassic and Cretaceous stratigraphy of the Huangshan Area, Anhui Province. Journal of Stratigraphy, 41, 209–215 (in Chinese with English abstract). doi: 10.19839/j.cnki.dcxzz.2017.02.010.

Ren XX, Huang JD, Liu J, Bi ZG. 2015. Late Jurassic volcanics

discovered in the Tunxi area of south Anhui. Geology of Anhui, 25, 241–244 (in Chinese with English abstract).

Ren XX, Huang JD, You HL. 2018. The second mamenchisaurid dinosaur from the Middle Jurassic of Eastern China. Historical Biology, 32(5), 1–9. doi: 10.1080/08912963.2018.1515935.

Ren XX, Jiang S, Wang XR, Peng GZ, Ye Y, Jia L, You HL. 2023. Re-examination of *Dashanpusaurus dongi* (Sauropoda: Macronaria) supports an early Middle Jurassic global distribution of neosauropod dinosaurs. Palaeogeography, Palaeoclimatology, Palaeoecology, 610, doi: 10.1016/j.palaeo.2022.111318.

Ren XX, Jiang S, Wang XR, Peng GZ, Ye Y, King L, You HL. 2022. Osteology of *Dashanpusaurus dongi* (Sauropoda: Macronaria) and new evolutionary evidence from Middle Jurassic Chinese sauropods. Journal of Systematic Palaeontology, 20: 1, 2132886, doi: 10.1080/14772019.2022.2132886.

Ren XX, Sekiya Y, Wang T, Yang ZW, You HL. 2021. A revision of the referred specimen of *Chuanjiesaurus anaensis* Fang et al., 2000: a new early branching mamenchisaurid sauropod from the Middle Jurassic of China. Historical Biology, 33(9), 1872–1887. doi: 10.1080/08912963.2020.1747450.

Sun SS, McDonough WF. 1989. Chemical and isotopic systematics of oceanic basalts: Implication for mantle composition and process. Geological Society, London, 313–345. doi: 10.1144/GSL.SP.1989.042.01.19.

Suteethorn S, Le Loeuff J, Buffetaut E, Sutteethorn V, Wongko K. 2013. Frist evidence of a mamenchisaurid dinosaur from the Upper Jurassic-Lower Cretaceous Phu Kradung Formation of Thailand. Acta Palaeontologica, 58, 459–469. doi: 10.4202/app.2009.0155.

Tang S, Xu XB, Yuan YM. 2016. Geochemistry and geochronology of the volcanic rocks from Tunxi basin in southern Anhui and their tectonic significance. Acta Petrologica ET Mineralogica, 35, 177–194 (in Chinese with English abstract).

Taylor SR, McLennan SM. 1985. The Continental Crust: Its Composition and Evolution. Oxford, Blackwell Scientific Publications, 57–72.

Wang TF. 2012. The tectonics of China. Beijing, Higher Education Press, 173–197 (in Chinese).

Wang Q, Xu JF, Jiao P, Bao ZW, Zhao ZH, Li CF, Xiong XL, Ma JL. 2006. Petrogenesis of adakitic porphyries in an extensional tectonic setting, Dexing, South China: Implications for the genesis of porphyry copper mineralization. Journal of Peterology, 47, 119–144 (in Chinese with English abstract). doi: 10.1093/petrology/egi070.

Wang QH. 2001. Discussion of ages of the Jiande group and the Moshishan group in Zhejiang. Volcanology & Mineral Resources, 22, 163–169 (in Chinese with English abstract).

Xie JC, Chen S, Rong W, Li QZ, Yang XY, Sun WD. 2012. Geochronology, geochemistry and tectonic significance of Guniujiang A-type granite in Anhui Province. Acta Petrologica Sinica, 28(12), 4007–4020 (in Chinese with English abstract). doi: 10.1134/S0869593812070027.

Xing LD, Miyashita T, Zhang JP, Li DQ, Ye Y, Sekiya T, Wang FP, Currie PJ. 2015. A new sauropod dinosaur from the Late Jurassic of China and the diversity, distribution, and relationships of mamenchisaurids. Journal of Vertebrate Paleontology, 35, e889701. doi: 10.1080/02724634.2014.889701.

Xu XB, Tang S, Lin SF. 2016. Paleostress inversion of fault-slip data from the Jurassic to Cretaceous Huangshan Basin and implications for the tectonic evolution of southeastern China. Journal of Geodynamics, 98, 31–25. doi: 10.1016/j.jog.2016.03.013.

Xue HM, Wang YG, Ma F, Wang C, Wang DE, Zuo YL. 2009. Zircon U-Pb SHRIMP ages of the Taiping (calc-alkaline) – Huangshan (alkaline) composite intrusive: Constraints on Mesozoic lithospheric thinning of the southeastern Yangtze craton, China. Science in China (Series D), 52(11), 1756–1770 (in Chinese with English abstract). doi: CNKI:SUN:JDXK.0.2009-07-010.

Yang QK, Zhang XL, Hua C, Yu, YS, Zhou WP. 2019. Petrogenic and metallogenic geochronology and its geological significance of the Dawangshan quartz vein type scheelite-molybdenite polymetallic deposit in central Jiangxi Province. Geophysical and Geochemical Exploration, 43(3), 558–567 (in Chinese with English abstract). doi: 10.11720/wtyht.2019.1478.

Yang SY, Liang JP, Jiang SY, Zhang X, Zhang RX. 2021. Late Jurassic–Early Cretaceous irregular slab rollback of paleo-Pacific plate beneath southeastern China: Insights from the petrogenesis of volcanic rocks of Moshishan Group in Dazhou volcanic basin, Gan-Hang Belt. Lithos, 392–393, 106137. doi: 10.1016/j.lithos.2021.106137.

Ye Y, Ouyang H, Fu QM. 2001. New material of *Mamenchisaurus hochuanensis* from Zigong, Sichuan. Vertebrata PalAsiatica, 39(4), 266–271 (in Chinese with English abstract). doi: 10.19615/j.cnki.1000-3118.2001.04.003.

Young CC. 1939. On a new Sauropoda, with notes on other fragmentary reptiles from Szechuan. Bulletin of the Geological Society of China, 279–235. doi: 10.19762/j.cnki.dizhixuebao.1939.03.005.

Young CC. 1958. New sauropods from China. Vertebrata Palasiatica, 2, 1–29.

Young CC, Chao XJ. 1972. *Mamenchisaurus Hochuanensis*. Beijing, Science Press, 1–30.

Yu XQ, Chen ZW, Liu X, Ji X, Zhou SZ, Yang XP. 2016. LA–ICP–MS zircon age of volcanic rock of Shiling Formation in Tunxi area, south Anhui, and redetermination of its epoch. Geological Bulletin of China, 35(1), 175–180 (in Chinese with English abstract).

Yu XQ, Zhang D, Wang LW, Yan TZ, Deng GH. 2006. Features of Caledonian tectonic deformation in the Zhejiang–Anhui–Jiangxi border region, China. Geological Bulletin of China, 25, 676–684 (in Chinese with English abstract).

Zhang Q, Chen Y, Zhou DJ, Qian Q, Jia XQ, Han S. 1998. Geochemical characteristics and genesis of Dachadaban ophiolite in North Qilian area. Science in China Series D: Earth Sciences, 41, 277–281 (in Chinese with English abstract). doi: 10.1007/BF02973116.

Zhang S, Zhang ZC. 2010. Petrology and geochemistry of the Huangshan granitic intrusion in Anhui Province, Southeast China: Implications for petrogenesis and geodynamics. Acta Geologica Sinica, 84(3), 581–596 (in Chinese with English abstract). doi: 10.1111/j.1755-6724.2010.00201.x.

Zhao JH, Zhou MF, Yan DP, et al. 2011. Reappraisal of the ages of Neoproterozoic strata in South China: no connection with the Grenvillian orogeny. Geology, 39(4), 299–302 doi: 10.1130/G31701.1.

Zhou J, Jiang YH, Ge WY. 2014. High Sr/Y Jingde pluton in the Eastern Jiangnan orogen, South China: formation Mechanism and tectonic implications. Acta Geologica Sinica, 88(1),

Zhou Q, Jiang YH, Liao SY, Zhao P, Jin GD, Jia RY, Liu Z, Xu SM. 2012. SHRIMP zircon U-Pb dating and Hf isotope studies of the diorite porphyrite from the Dexing copper deposit. Acta Geologica Sinica, 86(11), 1726–1734 (in Chinese with English abstract). doi: 10.1007/s11783-011-0280-z.

Zhu G, Liu GS. 2000. Basic characteristics and Mesozoic orogenic process of the Jiangnan Intercontinental Orogenic Belt in southern Anhui. Geotectonica et Metallogenia, 24, 103–111 (in Chinese with English abstract).